

# Inner-outer decomposition and universal near-wall motions in turbulent channels

Limin Wang<sup>1,2</sup>, Ruifeng Hu<sup>1,2</sup>, and Xiaojing Zheng<sup>1,2,3</sup>

<sup>1</sup>Key Laboratory of Mechanics on Disaster and Environment in Western China, Ministry of Education, Lanzhou University, Lanzhou 730000, China

<sup>2</sup>Department of Mechanics and Engineering Sciences, College of Civil Engineering and Mechanics, Lanzhou University, Lanzhou 730000, China

<sup>3</sup>Research Center for Applied Mechanics, School of Mechano-Electronic Engineering, Xidian University, Xi'an 710071, China

(Received xx; revised xx; accepted xx)

Near-wall turbulent velocities in turbulent channel flows are decomposed into small-scale and large-scale components at  $y^+ < 100$ , where  $y^+$  is the viscous-normalized wall-normal height. The small-scale one is obtained by fully removing outer influences and can be reminiscent of the well-known near-wall turbulence cycle. On the other hand, the large-scale one represents the near-wall footprints of outer energy-containing motions. We present plenty of evidences that demonstrate the small-scale motions are universal (Reynolds-number invariant) with the viscous scaling, at friction Reynolds numbers between 1000 and 5200. At lower Reynolds numbers from 180 to 600, the small scales can not be scaled by the viscous units, and the vortical structures are progressively strengthened as Reynolds number increases, which is proposed as the main mechanism responsible for the anomalous scaling behavior. The viscous-scaled energetic significance and length scales of outer footprints grow with Reynolds number, but their small-scale parts can be approximately scaled by the viscous units, implying possible relations with the inherently near-wall motions. Finally, the average effect of amplitude modulation may be negligible at least at the Reynolds numbers we consider, since the statistics of the small-scale velocities before and after the demodulation procedure are almost identical. The finding of the universal small-scale motions in wall turbulence may be akin to the universal small scales in homogeneous and isotropic turbulence, possibly suggesting the universality of the existence of universal small-scales in different turbulent flows.

## 1. Introduction

Reynolds-number dependence and scaling laws for mean and fluctuating values of flow quantities have always been being one of the most fundamental topics in turbulence research. For wall-bounded turbulent flows, the celebrated law of the wall for mean streamwise velocity is well known, albeit the debate on the logarithmic and the power laws (Marusic *et al.* 2010*b*). For turbulence quantities, Townsend (1976) proposed the attached eddy hypothesis (AEH) and predicted scaling relationships of fluctuating velocity variances at high-Reynolds-number condition, where it was postulated that the logarithmic layer of turbulent flow can be modelled as an ensemble of self-similar energy-containing eddies. The size and population density of these eddies are presumed to be proportional and inversely proportional to their wall normal height  $y$  (Perry & Chong 1982; Hwang & Sung 2018; Marusic & Monty 2019), respectively. There also exist a number of other theories in the literature that aim to predict the Reynolds-number effect and scaling laws of wall turbulence quantities (Monkewitz & Nagib 2015; Chen

*et al.* 2018, 2019). In the near-wall region, it is now well recognized that the peak of streamwise turbulence intensity has a weak Reynolds number dependence when it is scaled by the friction velocity  $u_\tau$  (De Graaff & Eaton 2000; Marusic *et al.* 2017), where  $u_\tau = \sqrt{\bar{\tau}_w/\rho}$  ( $\bar{\tau}_w$  is the mean wall-shear stress and  $\rho$  is the fluid density). Although the mean flow is well accepted to follow the law of the wall, there is less consensus about the scaling of the Reynolds normal stresses, especially the Reynolds-number dependence of the near-wall peak and its physical origins.

Reynolds-number effect on near-wall turbulence statistics has been explored in many investigations over the past several decades. The classical view of wall-bounded turbulence considers an inner region near the wall where the viscous effect dominates, so that all velocity statistics should be universally scaled by the friction velocity and the kinematic viscosity of the fluid (Tennekes & Lumley 1972). This is referred as the inner or viscous scaling that leads to the classical Prandtl's law of the wall. Although some studies seem to support this hypothesis (Perry & Abell 1975; Mochizuki & Nieuwstadt 1996; Tachibana *et al.* 2003; Hultmark *et al.* 2012; Vallikivi *et al.* 2015*b*), much more evidence definitely shows an increasing trend of the (inner) peak turbulence intensity with Reynolds number. The existence of Reynolds-number effect on near-wall turbulence intensities have been observed from numerous simulations and experiments in various types of canonical wall-bounded flows, including boundary layers, channels and pipes, which have provided strong evidence that near-wall turbulence statistics of fluctuating quantities do not follow the inner scaling (Purtell *et al.* 1981; Spalart 1988; Wei & Willmarth 1989; Erm & Joubert 1991; Antonia *et al.* 1992; Antonia & Kim 1994; Ching *et al.* 1995; De Graaff & Eaton 2000; Metzger & Klewicki 2001; Morrison *et al.* 2004; Hoyas & Jiménez 2006; Hutchins & Marusic 2007*a*; Schultz & Flack 2013; Vincenti *et al.* 2013; Bernardini *et al.* 2014; Lee & Moser 2015; Willert *et al.* 2017; Hu & Zheng 2018; Samie *et al.* 2018). There have been some excellent reviews on the Reynolds-number scaling issue which provide much more historical details (Gad-el Hak & Bandyopadhyay 1994; Fernholz & Finley 1996; Klewicki 2010; Marusic *et al.* 2017). Besides, several works attempted to reveal the physical mechanism responsible for the Reynolds-number dependence of near-wall turbulence statistics. For example, Wei & Willmarth (1989) measured the streamwise and wall-normal velocity components  $u$  and  $v$  with a laser-Doppler anemometer system in a turbulent channel flow and showed a systematic dependence of turbulence statistics on Reynolds number. They hypothesized that it may be a result of modifications of coherent structures in the vicinity of the wall, and suggested two possible mechanisms. The first one is an increase in near-wall vortex stretching with Reynolds number. The second one raises possibility of effect from the opposite wall, especially at low Reynolds number. Antonia *et al.* (1992) investigated the mechanism by introducing heating at one channel wall, and no strong evidence was found for direct interaction between inner regions of the opposite walls. It was further suggested that the Reynolds number effects of various turbulence quantities were likely to be associated with the increased intensities and stretching of quasi-streamwise vortices in the near-wall region (Antonia & Kim 1994).

In recent years, a prominent view is that the augmentation of near-wall turbulence intensities with Reynolds number can be attributed to the increasing influence of outer energetic motions in the inner region (Smits *et al.* 2011; Marusic *et al.* 2017). As Reynolds number increases, very long and energy containing motions prevail in the logarithmic layer of wall-bounded turbulent flows, and they are conventionally termed as large-scale motions (LSMs), very-large-scale motions (VLSMs), superstructures or global modes (Kovaszny *et al.* 1970; Brown & Thomas 1977; Kim & Adrian 1999; Del Álamo *et al.* 2004; Hutchins & Marusic 2007*a*; Lee & Sung 2011). It was found that the turbulence

kinetic energies carried by these structures increase with Reynolds number (Hoyas & Jiménez 2006; Balakumar & Adrian 2007; Hutchins & Marusic 2007*a*; Vallikivi *et al.* 2015*a*). The studies of Del Álamo & Jiménez (2003), Abe *et al.* (2004) and Hutchins & Marusic (2007*a*) among others have clearly demonstrated that the aforementioned large outer energetic motions can penetrate deep down to the wall, playing as strong imprints or footprints, which is also consistent with Townsend's AEH. As a consequence, the presence of large-scale footprints in the near-wall region can be associated with the failure of inner scaling of near-wall turbulence intensities (Marusic *et al.* 2017).

On the other hand, another major progress recently in wall turbulence research is the discovery of a self-sustaining near-wall regeneration cycle, which comprises of quasi-cyclic regeneration of streaks and quasi-streamwise vortices (Hamilton *et al.* 1995; Waleffe 1997; Kawahara & Kida 2001; Schoppa & Hussain 2002). In this process, streaks can be profoundly amplified by quasi-streamwise vortices through transferring energy of mean shear to streamwise velocity fluctuations, i.e., the so-called lift-up effect (Ellingsen & Palm 1975; Landahl 1990; Butler & Farrell 1993; Brandt 2014). Then the amplified streaks rapidly oscillate and break down due to instability or transient growth, which in turn leads to the generation of new quasi-streamwise vortices (Hamilton *et al.* 1995; Schoppa & Hussain 2002). This cycle can also be uncovered via nonlinearly equilibrium or temporally periodic invariant solutions of the incompressible Navier-Stokes equations, which are termed by the exact coherent states as well (Waleffe 1997; Kawahara & Kida 2001; Waleffe 2001). In addition, the near-wall cycle is found to be autonomous in that it could be well self-sustained by artificially removing outer turbulent fluctuations (Jiménez & Pinelli 1999). Therefore, it should be reasonable to hypothesize that the statistics of the near-wall cycle can be completely scaled with the viscous units and thus Reynolds-number invariant (Mathis *et al.* 2011), since it is now increasingly recognized that the Reynolds-number dependence of near-wall turbulence is solely introduced by outer footprints.

Based on the current understanding of near-wall turbulence, Marusic and co-workers proposed an algebraic predictive model for near-wall turbulence statistics with outer inputs (Marusic *et al.* 2010*a*; Mathis *et al.* 2011; Baars *et al.* 2016), by incorporating the effects of superposition (footprints) and amplitude modulation of outer large scales on inner small-scale turbulent motions (near-wall cycle). Hence it suggests that outer footprints and near-wall autonomous cycle co-exist and interact in the near-wall region. In their model, a universal small-scale velocity component, namely  $u^*$ , is supposed to be a surrogate of the near-wall cycle and should be determined *a priori* in a calibration measurement. The input large-scale velocity signal is measured at the centre of the logarithmic layer where the outer fluctuation is the strongest. The details of the model will be given in §3. The model has been demonstrated to work well at quite high Reynolds numbers (Mathis *et al.* 2011; Baars *et al.* 2016). For instance, the universal velocity signal  $u^*$  was acquired in turbulent boundary layer measurement at  $Re_\tau = 7300$  in Mathis *et al.* (2011), and predictions at  $Re_\tau = 2800 \sim 19000$  show reasonable agreements with the direct laboratory measurement data. Here the friction Reynolds number is defined by  $Re_\tau = u_\tau \delta / \nu$ ,  $u_\tau$  is the friction velocity,  $\delta$  is the outer length scale (boundary layer thickness, channel half height or pipe radius), and  $\nu$  is the fluid kinematic viscosity. Similar results were obtained by Baars *et al.* (2016) with a refined predictive model using a spectral linear coherence estimation instead of a definite spectral cut off. However, in practical implementation of the model, Mathis *et al.* (2011) claimed that the Fourier phases of the large-scale signal in the calibration measurement need to be retained and replace the large-scale velocity phases measured under the prediction condition. Without this procedure, one-point moments, especially high order ones, would be erroneously

predicted. This indicates that the extracted universal signal  $u^*$  may still contain a fraction of outer large-scale footprints (W. J. Baars, private communication).

The predictive model of Marusic and co-workers provides a natural decomposition of near-wall streamwise fluctuating velocity into small-scale and large-scale components. However, explicit assessment of Reynolds-number invariance of  $u^*$  was never put out. Moreover, there are some other relevant studies that tried to extract universal near-wall turbulence. Hwang (2013) designed numerical experiments that the near-wall turbulent motions with  $\lambda_z^+ > 100$  at  $Re_\tau$  up to 660 were removed using the spanwise minimum flow unit (MFU) of Jiménez & Moin (1991). It was found that the streamwise velocity fluctuations at  $y^+ < 40$  are well scaled by the viscous units, whereas the wall-normal and spanwise velocity fluctuations are not. Yin *et al.* (2017) extended the work of Hwang (2013) to higher Reynolds numbers, i.e.,  $Re_\tau = 1000 \sim 4000$ , confirming similar findings. Then Yin *et al.* (2018) modified the predictive model of Marusic and co-workers by replacing experimentally calibrated  $u^*$  with three-dimensional turbulent velocity fields obtained from MFU simulation. Yin *et al.* (2018) also compared the intensities of the extracted ( $u^*$ ,  $v^*$ ,  $w^*$ ) from the predictive model and MFU, and found good agreements at  $y^+ < 50$ , while the comparison was taken only at a single not a wide range of Reynolds number. Hearst *et al.* (2018) utilized a windowing technique to extract the universal inner small-scale spectrum measured from turbulent boundary layers subjected to high-intensity freestream turbulence, however this method may not be applied to instantaneous flow field. Carney *et al.* (2019) proposed an interesting near-wall patch approach, while which needs explicit high-pass filtering to obtain Reynolds-number invariant solutions.

Although some kind of success in extracting universal near-wall turbulence or application of the near-wall predictive models has been reported, several open issues still remain and need to be addressed. For example, is the  $u^*$  extracted from the predictive model actually Reynolds-number independence in a wide range of Reynolds number? What about the other two velocity components? Per the celebrated K41 theory for homogeneous and isotropic turbulence (Kolmogorov 1941), the universality of small scales has been widely regarded as one theoretical breakthrough and basis of modern statistical theory of turbulence (Frisch 1995). We believe it will also be of theoretical significance if universal small scales could be extracted in wall-bounded turbulence, and it is one major objective of the present study. Another objective is to reveal the characteristics and scalings of the large scales and their interactions with the small scales.

The paper is organised as follows. In §2, the data sets used in this work are described and the consistency is checked. In §3, we outline the decomposition scheme for extracting the universal small-scale motions of all three velocity components. Section §4 shows the main results, including the evidence of Reynolds-number independent universal small-scale motions in the Reynolds number range of  $Re_\tau = 1000 \sim 5200$ , and small scales with low-Reynolds-number effect at  $Re_\tau = 180 \sim 600$ , as well as the characteristics and scalings of large-scale footprints and inter-scale interactions. The final conclusion of the paper is drawn in §5.

## 2. Data sets

### 2.1. Data sources

The data sets used in this study are from DNS (direct numerical simulation) of fully developed turbulent channel flows, which are one of the most common canonical wall-bounded turbulent flows, sharing many similarities with boundary layer and pipe flows

TABLE 1. Summary of DNS data sets.  $L_x$  and  $L_z$  are computation domain sizes in streamwise and spanwise, respectively. The outer length scale, i.e., boundary-layer thickness, channel half height or pipe radius, is denoted by  $\delta$ .  $\Delta x^+$  and  $\Delta z^+$  are the streamwise and spanwise viscous-scaled grid size.  $\Delta y_w^+$  and  $\Delta y_c^+$  are the viscous-scaled wall-normal grid spacings at the wall and the channel centre, respectively.  $N_y$  is the grid number in the wall-normal direction. FD denotes finite difference scheme, and SP denotes spectral method.

$Re_\tau$	Method	$L_x/\delta$	$L_z/\delta$	$\Delta x^+$	$\Delta z^+$	$\Delta y_w^+$	$\Delta y_c^+$	$N_y$	Line and Symbols
180	FD	$8\pi$	$3\pi$	10	4.99	0.196	7.08	128	—●—
310	FD	$6\pi$	$2\pi$	10	5.00	0.270	9.84	160	—◆—
600	FD	$4\pi$	$2\pi$	10	5.00	0.325	11.97	256	—▲—
1000	SP	$8\pi$	$3\pi$	12.27	6.135	0.0165	6.155	512	—▼—
2000	SP	$8\pi$	$3\pi$	8.18	4.09	0.323	8.89	633	—▶—
5200	SP	$8\pi$	$3\pi$	12.76	6.38	0.498	10.3	1536	—★—

especially in the near-wall region, although differences exist more apparently in the outer region. The friction Reynolds numbers of the data sets are  $Re_\tau = 180, 310, 600, 1000, 2000$  and  $5200$ , covering a wide range over at least one order of magnitude, which could help to display the Reynolds number effect on the near-wall turbulence clearly.

The turbulent channel data sets at  $Re_\tau=180, 310$  and  $600$  are obtained from the DNS by ourselves. The DNS code adopts a fourth-order accurate compact difference scheme in the homogeneous directions and a second-order accurate central difference scheme in the wall-normal direction for the discretization of the incompressible Navier-Stokes equations on a staggered grid (Hu *et al.* 2018). The exact projection method is used for velocity-pressure decoupling. For temporal advancement, the Adams-Bashforth scheme is implemented for the convection terms, and Crank-Nicolson scheme for the viscous terms is employed to permit large time steps. The pressure Poisson equation is solved efficiently by Fast Fourier Transformation (FFT). In our previous work, a series of low-Reynolds-number channel DNS (up to  $Re_\tau = 180$ ) were conducted using the code (Hu & Zheng 2018) and the results were well validated against Lee & Moser (2015). In this study, we perform simulations at two higher Reynolds numbers, i.e.  $Re_\tau = 310$  and  $600$ , following the same standard at the lower Reynolds numbers. The DNS data sets of channel flows at  $Re_\tau = 1000$  and  $5200$  are from the group at The University of Texas at Austin (UTA) (Lee & Moser 2015), the raw data of which are assessed from the Johns Hopkins Turbulence Database (JHTDB) (Graham *et al.* 2016). And the data set at  $Re_\tau = 2000$  is from the group at Universidad Polit3cnica de Madrid (UPM) (Hoyas & Jim3nez 2006). All the cases of  $Re_\tau = 1000, 2000$  and  $5200$  were solved using spectral method in the wall-parallel planes, and the UTA group adopted a 7th-order B-spline collocation method while the UPM group employed a seven-point compact finite difference scheme in the wall-normal direction. In the following, the mean flow velocity is expressed by capital letters. The streamwise ( $x$ ), wall-normal ( $y$ ), and spanwise ( $z$ ) velocity fluctuations are denoted as  $u, v$  and  $w$ , respectively. The superscript '+' indicates the viscous scaling, i.e. the normalization by the friction velocity  $u_\tau$  and the kinematic viscosity  $\nu$ . The angle brackets represent the spatio-temporal averaging in both the homogeneous directions and time. The detailed information of the data sets is listed in table 1.

## 2.2. Consistency of the data

Since we use DNS data from the three different sources, it should be necessary to check the consistency of the data. To achieve this, we compare the mean velocity profile and various turbulence statistics (Reynolds stress components, pre-multiplied spectra

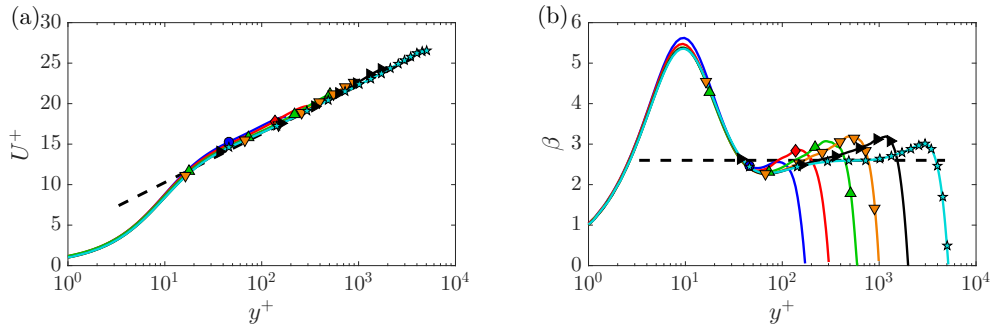


FIGURE 1. Mean streamwise velocity profiles (a) and log-law indicator function  $\beta$  (b) at  $Re_\tau = 180 \sim 5200$ . The dashed line in (a) denotes  $U^+ = (1/\kappa) \ln y^+ + B$ , where  $\kappa = 0.384$  and  $B = 4.27$ , and in (b) is  $\beta = 1/\kappa = 1/0.384 = 2.604$ .

and joint probability density functions) to inspect whether consistent Reynolds number dependence could be established from the data.

Mean streamwise velocity profile of turbulent wall-bounded flows has been studied extensively and a lot of theories have been proposed. The characteristic length scales of the near-wall flow and the outer flow are  $\nu/u_\tau$  and  $\delta$ , respectively. In the intermediately overlap region, both length scales are relevant, and the logarithmic law of mean streamwise velocity can be derived through dimensional analysis in this region (Millikan 1939). Figure 1 (a) shows the viscous-scaled mean streamwise velocity profiles at different Reynolds numbers. In general, the mean velocity profiles are observed to be well consistent among different data sets. It is known that the mean streamwise velocity in the most inner layer adjacent to the wall ( $y^+ \leq 5$ ) follows a linear relationship, i.e.  $U^+ = y^+$ , which is Reynolds number independent and favorably evidenced in figure 1 (a). In the overlap region, the mean velocity profile can be well approximated by the logarithmic law of the wall, as  $U^+ = (1/\kappa) \ln y^+ + B$ . Moreover, the parameter  $\beta(y^+) = y^+ (\partial U^+ / \partial y^+)$  can be used as an indicator function for the logarithmic law, which should be a constant ( $1/\kappa$ ) in the logarithmic region. As shown in figure 1 (b), a visible plateau region of  $\beta$  can be well observed in the highest Reynolds number case ( $Re_\tau = 5200$ ). The constants in the log law have been determined as  $\kappa \approx 0.384$  and  $B \approx 4.27$ , according to the fitting by Lee & Moser (2015) at  $Re_\tau = 5200$ . The log-law region is not very evident at lower Reynolds numbers, therefore some studies attempted to consider higher-order truncation of matched asymptotic expansions of  $\beta$  in terms of  $y^+$  and  $1/Re_\tau$  (Afzal & Yaajnik 1973; Jiménez & Moser 2007; Mizuno & Jiménez 2011). Nevertheless, we will not go any further for the mean velocity profile.

Next, we focus on Reynolds stress components that include the Reynolds normal stresses or the turbulence intensities in the three Cartesian directions ( $\langle u^2 \rangle^+$ ,  $\langle v^2 \rangle^+$  and  $\langle w^2 \rangle^+$ ) as well as the Reynolds shear stress ( $\langle uv \rangle^+$ ), which are shown in figure 2 (a, b, c, d). It is clearly seen that these second-order statistics have consistent behaviors with respect to  $y^+$  and  $Re_\tau$ , further showing the adequacy of the data sets from different sources. In addition, figure 2 (e) displays the variation of  $\langle u^2 \rangle_{\max}^+$  (the peak value of  $\langle u^2 \rangle^+$ , located at  $y^+ \approx 15$ ) with Reynolds number  $Re_\tau$ , and our low-Reynolds-number channel DNS data are well consistent with the higher-Reynolds-number data of Lee & Moser (2015) and Hoyas & Jiménez (2006). The turbulent boundary layer measurement data in the Melbourne Wind Tunnel (MWT) (Marusic *et al.* 2015) is also included in figure 2 (e). It is worth noting that  $\langle u^2 \rangle_{\max}^+$  in both channel and boundary layer flows can be properly fitted with  $Re_\tau$  using a logarithmic relationship, as  $\langle u^2 \rangle_{\max}^+ = 3.66 + 0.642 \ln Re_\tau$  (Lee &

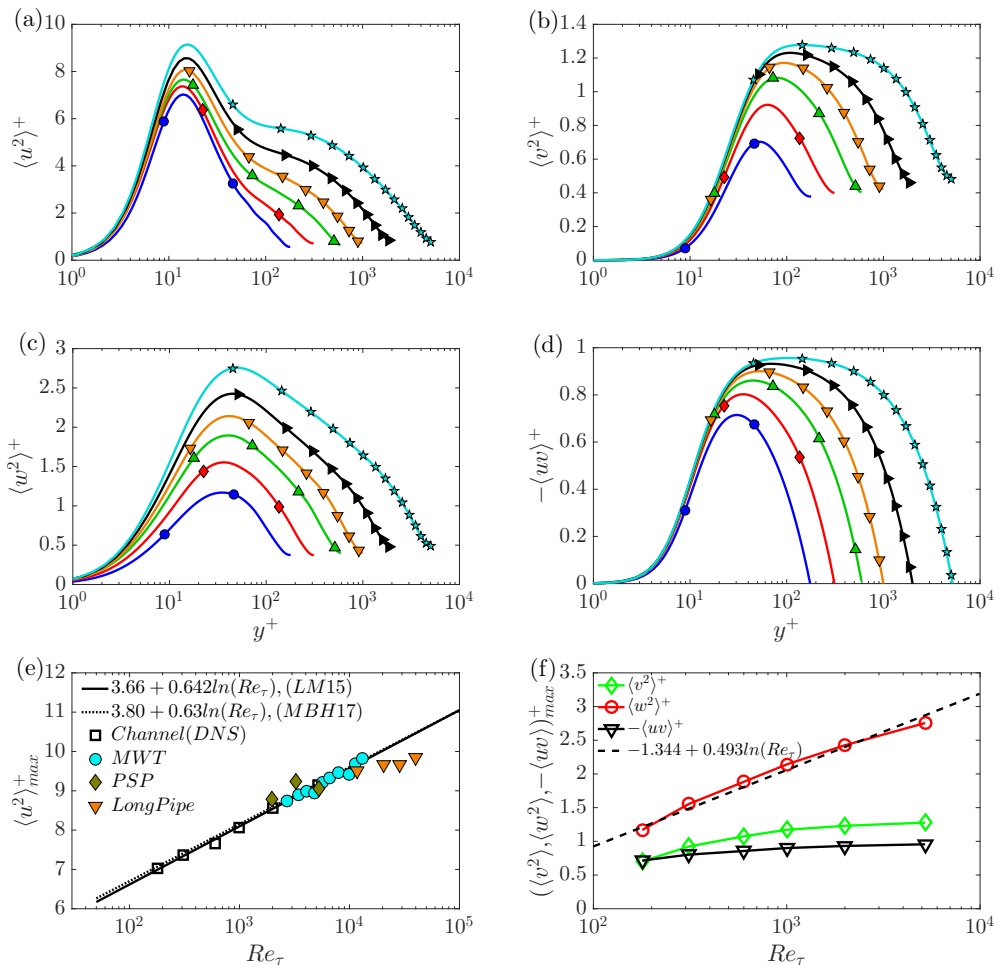


FIGURE 2. Wall-normal profiles of Reynolds stress components and Reynolds number dependence of the peak values: (a)  $\langle u^2 \rangle^+$ ; (b)  $\langle v^2 \rangle^+$ ; (c)  $\langle w^2 \rangle^+$ ; (d)  $-\langle uv \rangle^+$ ; (e) the  $Re_\tau$  dependence of  $\langle u^2 \rangle_{\max}^+$ ; LM15 denotes Lee & Moser (2015) and MBH17 denotes Marusic *et al.* (2017); MWT is the boundary layer measurements in the Melbourne Wind Tunnel (Marusic *et al.* 2015); PSP is the Princeton Superpipe measurements (Hultmark *et al.* 2010, 2012); LongPipe is the CICLoPE Long pipe measurements (Willert *et al.* 2017); (f) the  $Re_\tau$  dependence of the peak values of  $\langle v^2 \rangle^+$ ,  $\langle w^2 \rangle^+$  and  $-\langle uv \rangle^+$ .

Moser 2015) or  $\langle u^2 \rangle_{\max}^+ = 3.80 + 0.63 \ln Re_\tau$  (Marusic *et al.* 2017), which almost coincide with each other. To be more complete, the  $\langle u^2 \rangle_{\max}^+$  values in turbulent pipe flows from the measurements of Princeton Superpipe (Hultmark *et al.* 2010, 2012) and CICLoPE Long pipe (Willert *et al.* 2017) are also included in figure 2 (e), from which we can see that the maximum streamwise turbulence intensity in pipe flow also increases with  $\ln Re_\tau$  in an approximately linear manner while at a smaller slope. Figure 2 (f) shows the Reynolds number dependence of the peak values of the other Reynolds stress components, i.e.  $\langle v^2 \rangle^+$ ,  $\langle w^2 \rangle^+$  and  $-\langle uv \rangle^+$ . We can see that the peak magnitude of spanwise turbulence intensity has a similar logarithmic increasing trend as the streamwise one, and an empirical fitting expression is proposed here as  $\langle w^2 \rangle_{\max}^+ = 1.344 + 0.493 \ln Re_\tau$ . The peaks of  $\langle v^2 \rangle^+$  and

$\langle -uv \rangle^+$  slightly increase with Reynolds number and seem to be able to reach asymptotic values when  $Re_\tau$  is high enough.

According to the attached-eddy hypothesis of Townsend (1976), the Reynolds stress components are predicted to satisfy the following scaling relationships in the logarithmic layer of wall-bounded turbulent flows,

$$\langle u^2 \rangle^+ = A_1 - B_1 \log(y/\delta), \quad (2.1)$$

$$\langle w^2 \rangle^+ = A_3 - B_3 \log(y/\delta), \quad (2.2)$$

$$\langle v^2 \rangle^+ = B_2, \quad \langle uv \rangle^+ = -1. \quad (2.3)$$

For the streamwise turbulence intensity  $\langle u^2 \rangle^+$ , as displayed in figure 2 (a), the log law (2.1) can hardly be detected at the low to moderate Reynolds numbers (Jiménez & Hoyas 2008; Sillero *et al.* 2013; Bernardini *et al.* 2014; Lee & Moser 2015; Hu & Zheng 2018), unless at enough high Reynolds numbers (Hultmark *et al.* 2012; Marusic *et al.* 2013; Yamamoto & Tsuji 2018; Samie *et al.* 2018). It should be mentioned that recent studies including ours indicate that the log law of  $\langle u^2 \rangle^+$  can hold at lower Reynolds numbers if the part of the wall-attached eddies could be extracted from the total fluctuations (Baars & Marusic 2020*b*; Hu *et al.* 2020). Nonetheless, the spanwise turbulence intensity can obey the log law (2.2) at much lower Reynolds numbers (Jiménez & Hoyas 2008; Bernardini *et al.* 2014; Yang *et al.* 2018; Mehrez *et al.* 2019), as shown in figure 2 (c). From figure 2 (b, d), it appears that wider plateau regions of both  $\langle v^2 \rangle^+$  and  $\langle -uv \rangle^+$  are emerging as the Reynolds number increases, which is also supported by the Reynolds number dependence of their maximum values in figure 2 (f).

Thirdly, we move on to the scale-to-scale measures of turbulence kinetic energies in the three directions and the corresponding Reynolds number effects. The analysis tool of pre-multiplied energy spectrum is intensely used here, which can effectively aid to reveal the spectral energy distribution of turbulence fluctuations in the logarithmic coordinate. To be more specific, we exhibit the viscous-scaled pre-multiplied spectral energy densities (e.g.,  $k_x E_{uu}/u_\tau^2$ ) into a contour plot against viscous-scaled wavelength ( $\lambda_x^+ = \lambda_x/(\nu/u_\tau)$ ) and wall-normal height ( $y^+$ ). Here,  $E_{uu}$  is the spectral energy density of  $u$  at a wavenumber  $k_x$  or wavelength  $\lambda_x = 2\pi/k_x$ . The definitions for other velocity components and in the spanwise direction are similar and straightforward. This tool has been widely adopted for analyzing the scale-to-scale properties of turbulence fluctuations (Kim & Adrian 1999; Guala *et al.* 2006; Balakumar & Adrian 2007; Hutchins & Marusic 2007*a*; Hwang 2013, 2015; Lee & Moser 2015, 2019; Vallikivi *et al.* 2015*a*; Wang & Zheng 2016; Hu & Zheng 2018; Wang *et al.* 2018; Cheng *et al.* 2019; Wang *et al.* 2019*b*). Figure 3 shows the streamwise and spanwise pre-multiplied energy spectra of all the three components of velocity fluctuations. As Reynolds number increases, the viscous-scaled wall-normal range increases accordingly, resulting in the upwards extended contour patterns. In the near-wall region, i.e.  $y^+ < 100$ , distinct inner peaks can be clearly observed, which are the spectral signatures of predominant near-wall coherent structures (streaks, quasi-streamwise vortices, etc) with specific characteristic length scales. The streamwise and spanwise pre-multiplied energy spectra of streamwise velocity fluctuations  $k_x E_{uu}/u_\tau^2$  and  $k_z E_{uu}/u_\tau^2$  at  $Re_\tau = 180 \sim 5200$  are shown in figure 3 (a) and (b). The inner peak locates at  $y^+ = 10 \sim 20$ , with  $\lambda_x^+ \sim O(10^3)$  and  $\lambda_z^+ \sim O(10^2)$ , which is consistent with the well known characteristic streamwise length and spanwise spacing of near-wall streaks obtained from visualized measurements or DNS (Kline *et al.* 1967; Smith & Metzler 1983; Kim *et al.* 1987). In the near-wall small-scale region ( $y^+ < 40$ ,  $\lambda_x^+ < 7000$  or  $\lambda_z^+ < 200$ ), it is seen that the spectra at different  $Re_\tau$  collapse generally well, indicating Reynolds-

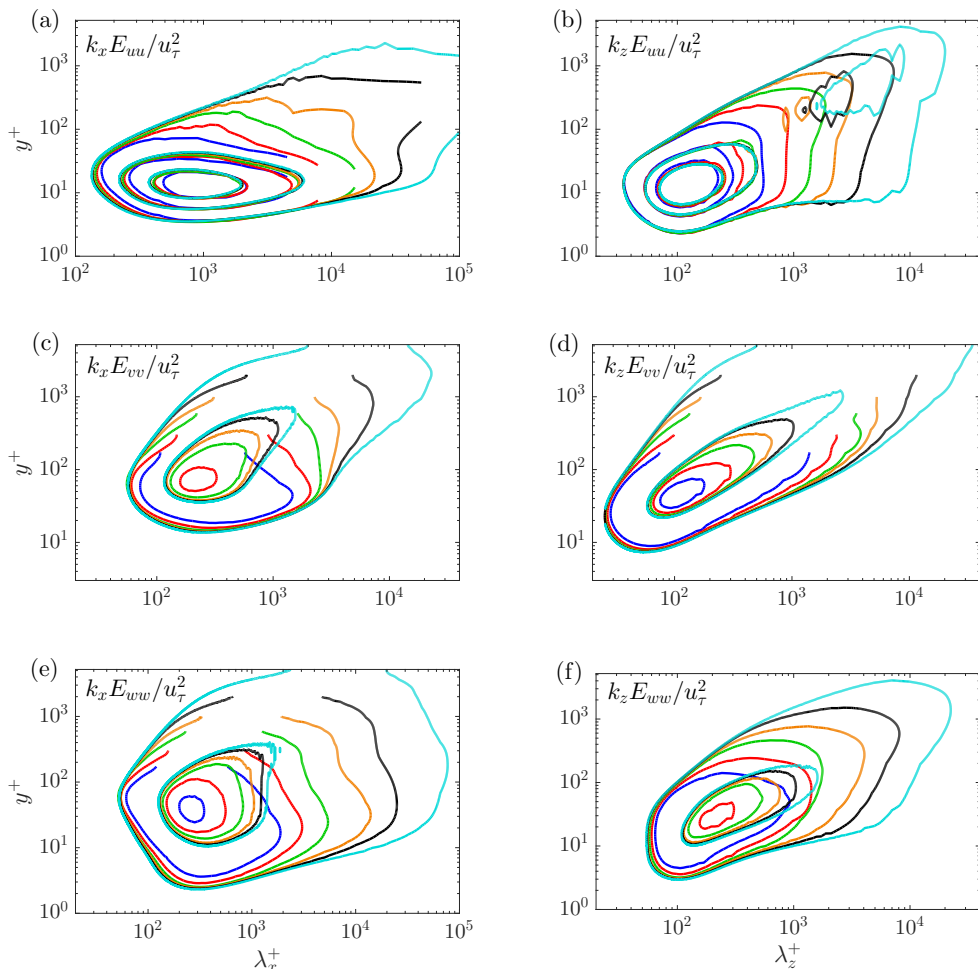


FIGURE 3. Pre-multiplied energy spectra of the three velocity components at different Reynolds numbers. The contour levels are (a) (0.6, 1.2, 1.8) for  $k_x E_{uu}/u_\tau^2$ ; (b) (0.5, 1.5, 2.5) for  $k_z E_{uu}/u_\tau^2$ ; (c) (0.1, 0.3) for  $k_x E_{vv}/u_\tau^2$ ; (d) (0.05, 0.35) for  $k_z E_{vv}/u_\tau^2$ ; (e) (0.1, 0.45) for  $k_x E_{ww}/u_\tau^2$ ; (f) (0.2, 0.6) for  $k_z E_{ww}/u_\tau^2$ .

number-independent universal near-wall turbulent motions, but they are not separated from the imprints of outer motions. However, it is noted that a certain degree of mismatch exists in the streamwise spectra, and the streamwise length of the inner peak is longer at lower Reynolds numbers, which has been reported in our previous low- $Re_\tau$  simulations (Hu & Zheng 2018). In contrast, we can hardly find collapsed near-wall viscous scalings for the pre-multiplied energy spectra of wall-normal and spanwise velocity components as good as the streamwise one, as displayed in figure 3 (c-f). In other words,  $v$  and  $w$  show evident Reynolds number dependence in the spectra. The wall-normal locations of the inner peaks of the  $v$ - and  $w$ -spectra are much higher, as  $y^+ = 30 \sim 70$ , since  $v$  and  $w$  are primarily induced by quasi-streamwise vortical structures which generally ride above near-wall streaks (Hwang 2013). For the last point, we observe that the spectral imprints of outer large-scale components into the near-wall region are stronger and extending to longer wavelength if  $Re_\tau$  is larger, demonstrating increasing outer influences, which is also consistent with many previous findings (Metzger & Klewicki 2001; Del Álamo &

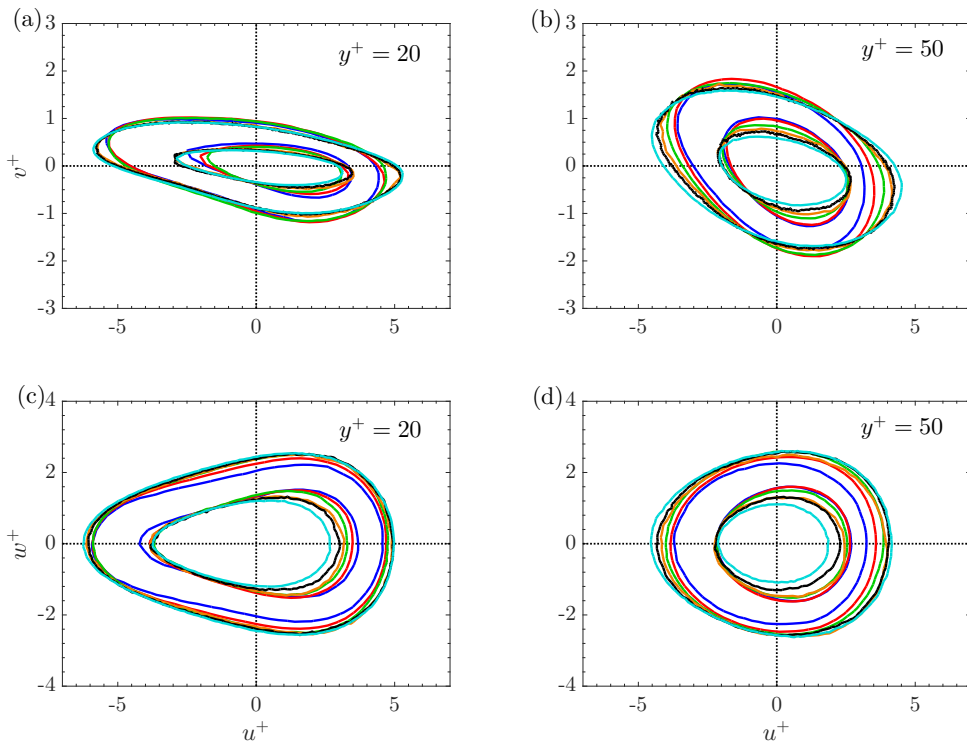


FIGURE 4. Joint p.d.f.s  $P(u^+, v^+)$  (a, b) and  $P(u^+, w^+)$  (c, d) at  $y^+ = 20$  (a, c) and  $y^+ = 50$  (b, d) in the fully developed turbulent channel flows at the Reynolds numbers  $Re_\tau = 180 \sim 5200$ . The contour levels are (0.2, 0.6) normalized by the peak value of the p.d.f. at  $Re_\tau = 1000$  of the two heights.

Jiménez 2003; Abe *et al.* 2004; Hutchins & Marusic 2007*b*; Morrison 2007; Mathis *et al.* 2009; Agostini & Leschziner 2014; Baars *et al.* 2015; Hwang *et al.* 2016; Hwang 2016; Lee & Moser 2019). And the major objective of the present study is to remove the large-scale imprints on the near-wall region and extract truly Reynolds-number-independent universal near-wall motions.

Lastly, we present the results of joint probability distribution functions (p.d.f.s) between velocity components, i.e.,  $P(u^+, v^+)$  and  $P(u^+, w^+)$  at  $y^+ = 20$  and  $y^+ = 50$ , which is shown in figure 4. The joint p.d.f.s are useful and can be applied to examine the most probable turbulent motions via the one-point velocity cross-correlations. For example, the quadrant analysis, proposed nearly fifty years before, has been thoroughly adopted to detect the outward (Q1,  $u > 0$  and  $v > 0$ ), ejection (Q2,  $u < 0$  and  $v > 0$ ), inward (Q3,  $u < 0$  and  $v < 0$ ) and ejection (Q4,  $u > 0$  and  $v < 0$ ) events (Wallace *et al.* 1972; Willmarth & Lu 1972; Lu & Willmarth 1973; Wallace 2016). As displayed in figure 4 (a, b), the shape of  $P(u^+, v^+)$  is inclined with the major axis in the Q2-Q4 direction, implying much higher probabilities of the ejection and sweep events. The p.d.f. contours at the two heights both show Reynolds number dependence, and the major axis tends to the  $v^+ = 0$  if  $Re_\tau$  increases, which indicates  $u^+$  increases more rapidly than  $v^+$ . If comparing the p.d.f.s at the two heights, i.e. figure 4 (a) and (b), it is seen that the inclination of the major axis is steeper at  $y^+ = 50$ , that means the ejecting and sweeping angles of coherent motions are smaller towards the wall. On the other hand, figure 4 (c, d) demonstrates that the shape of  $P(u^+, w^+)$  is symmetric about  $w^+ = 0$  in

all cases. However, the p.d.f.s are not symmetric about  $u^+ = 0$ , showing quite different velocity distributions at  $u > 0$  and  $u < 0$ . In general, the spanwise velocity  $w$  has a wider distribution at  $u > 0$  than  $u < 0$ . This is probably due to the splatting effect (Agostini & Leschziner 2014; Agostini *et al.* 2016; Pan & Kwon 2018) or the dispersive motions of high-speed structures (Hwang *et al.* 2016), i.e., high-speed sweeping (Q4) motions may be converted into spanwise motions near the wall since the wall is impermeable. The splatting/dispersive effect becomes weaker away from the wall, which could be confirmed in figure 4 (d). Also, there exists visible Reynolds number dependence of  $P(u^+, w^+)$ .

In summary, we have presented various statistics (Reynolds stress, pre-multiplied energy spectra and joint p.d.f.s) of the channel flow DNS from three different sources using different numerical methods, covering a wide range of Reynolds numbers with  $Re_\tau = 180 \sim 5200$ . All of the results support that the data sets are consistent with each other, showing reasonable Reynolds number dependence. In the following, we will employ the above DNS data to work out the decomposition of near-wall turbulent motions with confidence.

### 3. The decomposition methodology

The decomposition of near-wall turbulent motions is based on the framework of the predictive inner-outer (PIO) model proposed by Marusic and co-workers (Marusic *et al.* 2010*a*; Mathis *et al.* 2011). Here we resort to the refined PIO model of Baars *et al.* (2016), which eliminates the need for a specific spectral cut-off filter to separate small- and large-scale velocities as in the original version of this model. The basic idea of the PIO model is that the near-wall turbulence fluctuations could be decomposed into two components, i.e., the footprints or imprints of outer large-scale fluctuations (the superposition effect), and the small-scale fluctuations with modulated amplitudes by large scales (the modulation effect).

The refined PIO model takes the form of

$$u_p^+(y^+) = \underbrace{u^*(y^+) [1 + \Gamma_{uu}(y^+) u_L^+(y^+, y_O^+)]}_{\text{modulation}} + \underbrace{u_L^+(y^+, y_O^+)}_{\text{superposition}}. \quad (3.1)$$

Here  $u_p^+$  is the predicted streamwise fluctuating velocity near the wall ( $y^+ < 100$ ), and the dependence on the streamwise, spanwise coordinates ( $x^+$  and  $z^+$ ) and time ( $t^+$ ) are omitted for simplification. All of the variables are normalized by the viscous units. In the right-hand-side of equation (3.1),  $\Gamma_{uu}(y^+)$  is the modulation coefficient and  $u^*(y^+)$  is the near-wall universal signal in the absence of outer influence, which are usually determined through a synchronously two-point calibration experiment, and assumed to be universal at any Reynolds number (Mathis *et al.* 2011; Baars *et al.* 2016). The second term  $u_L^+(y^+, y_O^+)$  denotes the footprint of the outer large-scale fluctuating velocity  $u^+(y_O^+)$  at  $y_O^+$  on a near-wall position  $y^+$ , and  $y_O^+$  is usually chosen at the centre of the logarithmic layer (Mathis *et al.* 2011; Baars *et al.* 2016; Yin *et al.* 2018). Here we also follow Baars *et al.* (2016) to calculate the outer footprint velocity  $u_L^+(y^+, y_O^+)$  as

$$u_L^+(y^+, y_O^+) = F_x^{-1} \{ H_{Lu}(\lambda_x^+, y^+, y_O^+) F_x [u_O^+(y_O^+)] \}, \quad (3.2)$$

in which,  $u_O^+(y_O^+)$  is the input outer fluctuating velocity at  $y_O^+$ ,  $F_x$  and  $F_x^{-1}$  denote FFT and inverse FFT, respectively.  $H_{Lu}(\lambda_x^+, y^+, y_O^+)$  is a scale-dependent complex-valued kernel function depending on the streamwise wavelength and wall-normal position, representing the spectral linear stochastic estimation of outer streamwise velocity in the near-wall

region (Baars *et al.* 2016), which is defined by

$$H_{Lu}(\lambda_x^+, y^+, y_O^+) = \frac{\langle \hat{u}^+(\lambda_x^+, y^+) \overline{\hat{u}^+(\lambda_x^+, y_O^+)} \rangle}{\langle \hat{u}^+(\lambda_x^+, y_O^+) \overline{\hat{u}^+(\lambda_x^+, y_O^+)} \rangle} = |H_{Lu}| e^{j\phi}. \quad (3.3)$$

Here,  $\hat{u}^+ = F_x(u^+)$  is the Fourier transform of  $u^+$  along  $x$  direction, the overbar indicates complex conjugate and  $\phi$  is the phase difference of the two spectrum. Following Baars *et al.* (2016), we also use a bandwidth moving filter of 25% to smooth the original spectral transfer kernel  $H_{Lu}$ .

According to the above seminal works (Marusic *et al.* 2010a; Mathis *et al.* 2011; Baars *et al.* 2016), the determination procedure of statistically universal near-wall fluctuating streamwise velocity  $u^*$  as well as the modulation coefficient  $\Gamma_{uu}$  can be summarized as follows: (i) Calculate the kernel function  $H_{Lu}(\lambda_x^+, y^+, y_O^+)$  and the outer footprint velocity  $u_L^+(y^+, y_O^+)$  with given outer reference height  $y_O^+$  according to equation (3.2). (ii) Get the near-wall small-scale velocity by subtracting  $u_L^+(y^+, y_O^+)$  from the original one, i.e.  $u_S^+ = u^+ - u_L^+$ . (iii) De-modulate  $u_S^+$  to determine  $\Gamma_{uu}$  and  $u^*$  through an iterative procedure so that the amplitude modulation coefficient is zero. More details about the procedure can be found in Mathis *et al.* (2011) and Baars *et al.* (2016).

The original PIO model is only applied to the streamwise fluctuating velocity, here we simply extend it to all the three velocity components, since previous study has revealed strong similarities among them (Talluru *et al.* 2014). Consequently, the equations to determine the near-wall universal fluctuating velocity components can be written as

$$u^*(y^+) = \frac{u^+(y^+) - u_L^+(y^+, y_O^+)}{1 + \Gamma_{uu}(y^+) u_L^+(y^+, y_O^+)} = \gamma_{uu}(y^+) u_S^+(y^+, y_O^+), \quad (3.4)$$

$$v^*(y^+) = \frac{v^+(y^+) - v_L^+(y^+, y_O^+)}{1 + \Gamma_{uv}(y^+) u_L^+(y^+, y_O^+)} = \gamma_{uv}(y^+) v_S^+(y^+, y_O^+), \quad (3.5)$$

$$w^*(y^+) = \frac{w^+(y^+) - w_L^+(y^+, y_O^+)}{1 + \Gamma_{uw}(y^+) u_L^+(y^+, y_O^+)} = \gamma_{uw}(y^+) w_S^+(y^+, y_O^+), \quad (3.6)$$

where

$$\gamma_{uu}(y^+) = [1 + \Gamma_{uu}(y^+) u_L^+(y^+, y_O^+)]^{-1},$$

$$\gamma_{uv}(y^+) = [1 + \Gamma_{uv}(y^+) u_L^+(y^+, y_O^+)]^{-1},$$

$$\gamma_{uw}(y^+) = [1 + \Gamma_{uw}(y^+) u_L^+(y^+, y_O^+)]^{-1},$$

and

$$u_S^+(y^+, y_O^+) = u^+(y^+) - u_L^+(y^+, y_O^+),$$

$$v_S^+(y^+, y_O^+) = v^+(y^+) - v_L^+(y^+, y_O^+),$$

$$w_S^+(y^+, y_O^+) = w^+(y^+) - w_L^+(y^+, y_O^+).$$

Equation (3.4) is actually re-organized from equation (3.1). In the numerators of the right-hand-sides of the above equations,  $v_L^+(y^+, y_O^+)$  and  $w_L^+(y^+, y_O^+)$  are the wall-normal and spanwise outer footprint velocity components in the near-wall region, respectively, which are obtained similar to  $u_L^+(y^+, y_O^+)$ , using  $v$  and  $w$  instead of  $u$  in equations (3.2) and (3.3). The denominators are the modulators of the universal fluctuating velocity components, all of which use  $u_L^+$  to evaluate the amplitude modulation effect, following the suggestion of Talluru *et al.* (2014). The only difference is the modulation coefficients, i.e.  $\Gamma_{uu}$ ,  $\Gamma_{uv}$  and  $\Gamma_{uw}$ , which are determined separately in the three directions.

It should be mentioned that there have been several studies that attempted to extend the original PIO model including the other two velocity components. Agostini & Leschziner (2016) proposed a predictive model for the three-dimensional near-wall flow field at  $Re_\tau \approx 1000$  by invoking the general form of the PIO model, while the universal fluctuating velocities were extracted through the Empirical Mode Decomposition and taking account of the sweep-induced splattering effect. Yin *et al.* (2018) utilized the flow solution of the minimal flow unit (MFU) (Jiménez & Moin 1991) at  $Re_\tau \approx 2000$  as a surrogate of near-wall universal flow field, and also established a predictive model in the framework of the PIO model. Although the above two models could yield satisfied predictions at the Reynolds number the model parameters are determined, they did not demonstrate the predicting capability at other Reynolds numbers. What is more, whether the extracted universal near-wall flow field is really *universal*, i.e. Reynolds number invariant, was also not explicitly addressed.

## 4. Results and analysis

### 4.1. Universal near-wall motions

#### 4.1.1. Turbulence statistics

Now we present application results of the extracting scheme (3.4-3.6) for the near-wall universal velocity fields. The primary input is the outer reference height  $y_O^+$ , since the kernel functions ( $H_{Lu}, H_{Lv}, H_{Lw}$ ) and the imprint velocities ( $u_L^+, v_L^+, w_L^+$ ) can be directly calculated once  $y_O^+$  is given. In the majority of the previous studies,  $y_O^+$  is chosen at the centre of the logarithmic layer (Mathis *et al.* 2011; Inoue *et al.* 2012; Baars *et al.* 2016; Yin *et al.* 2018), i.e.  $y_O^+ \approx 3.9\sqrt{Re_\tau}$ , because the outer spectral peak of streamwise velocity fluctuations is located at this height (Hutchins & Marusic 2007a). Although generally good agreement of the extracted  $u^*$  statistics has been reported at high Reynolds numbers (Baars *et al.* 2016), we find the extracted near-wall motions from the channel DNS data are actually Reynolds number dependent (the results are not shown here). This indicates that the near-wall influence from a portion of outer motions may be still included, if we trust the inner-outer interaction hypothesis and choose  $y_O^+ \approx 3.9\sqrt{Re_\tau}$ . This could be true as Townsend (1976) already proposed that the wall-attached eddies can influence the near-wall flow, and the geometrically self-similar eddies with sizes of  $l_y^+ < 3.9\sqrt{Re_\tau}$  are probably active near the wall (Perry & Chong 1982). Therefore it reminds us that the truly universal near-wall fluctuations may be successfully extracted by gradually reducing the input reference height  $y_O^+$ .

In the following, the turbulence intensities of the extracted near-wall velocity fluctuations according to equations (3.4-3.6) are compared at the Reynolds numbers  $Re_\tau = 1000, 2000$  and  $5200$ , as shown in figure 5 (a, c, e). By systematically decreasing the reference height  $y_O^+$  from 300 to 200 and finally 100, it clearly shows that the extracted ( $\langle u^{*2} \rangle$ ,  $\langle v^{*2} \rangle$ ,  $\langle w^{*2} \rangle$ ) are less dependent on Reynolds number, if  $y_O^+$  is smaller. Furthermore, the Reynolds number invariant ( $\langle u^{*2} \rangle$ ,  $\langle v^{*2} \rangle$ ,  $\langle w^{*2} \rangle$ ) could be well defined with  $y_O^+ = 100$  and at  $Re_\tau = 1000 \sim 5200$ . In figure 5 (b, d, f), only the extracted ( $\langle u^{*2} \rangle$ ,  $\langle v^{*2} \rangle$ ,  $\langle w^{*2} \rangle$ ) with  $y_O^+ = 100$  at the three Reynolds numbers are displayed and excellent coincidence can be found, especially for  $\langle u^{*2} \rangle$  and  $\langle v^{*2} \rangle$ . However, it should be admitted that, the extracted spanwise turbulence intensity  $\langle w^{*2} \rangle$  is slightly dependent on  $Re_\tau$ , as shown in figure 5 (f). We have tried to further reduce  $y_O^+$ , but no better improvement can be achieved. It may be ascribed to the anti-correlation of spanwise velocity above and below the centre of a quasi-streamwise vortical structure. A lot of DNS and PIV measurements revealed that the low- and high-momentum regions in the outer region are flanked by a

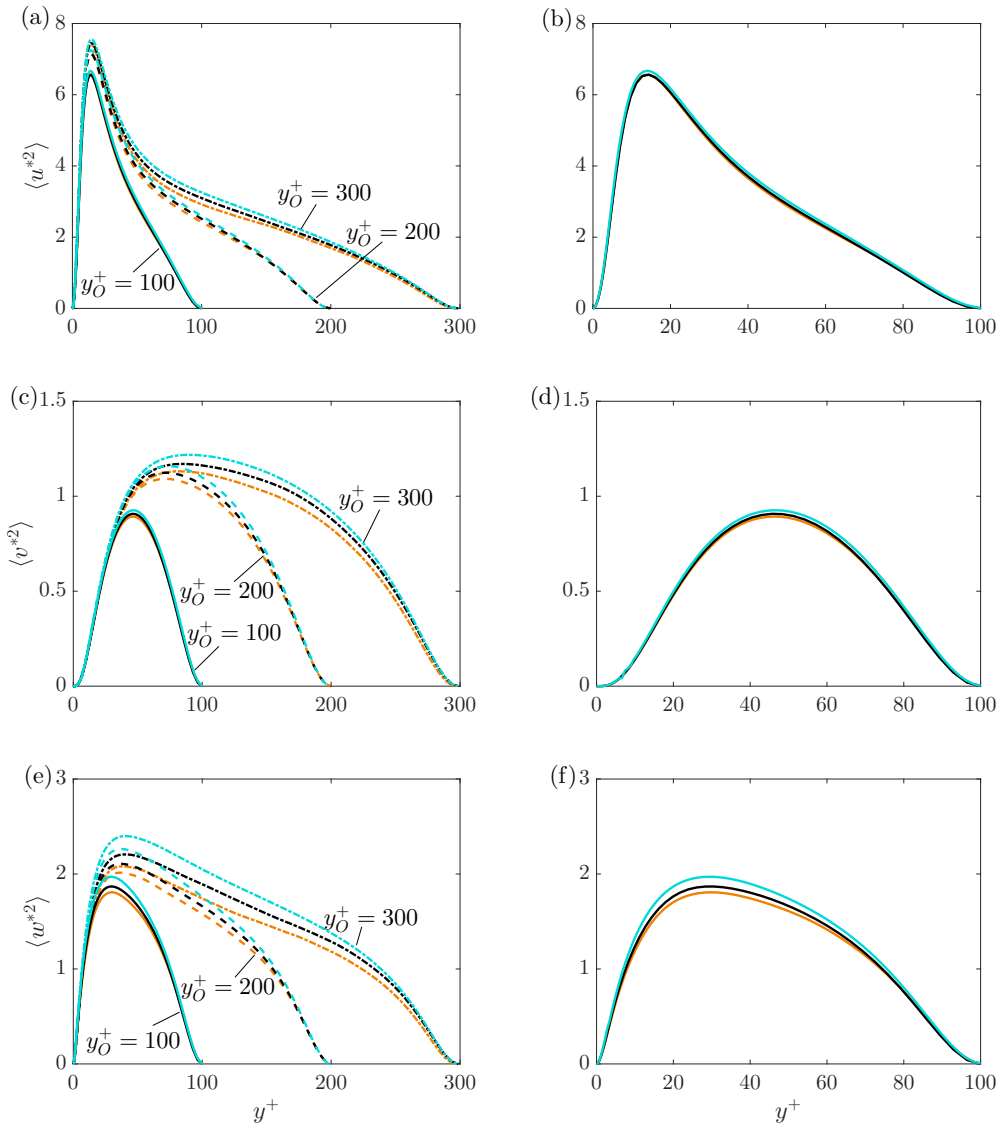


FIGURE 5. Turbulence intensities of the extracted universal fluctuating velocity components at  $Re_\tau = 1000, 2000$  and  $5200$ : (a, b) streamwise velocity; (c, d) wall-normal velocity; (e, f) spanwise velocity. In (a, c, e), the reference wall-normal position  $y_O^+$  varies from  $300$  to  $100$ :  $y_O^+ = 300$  (dot-dashed lines),  $y_O^+ = 200$  (dashed lines) and  $y_O^+ = 100$  (solid lines). In (b, d, f), only the results using the reference position  $y_O^+ = 100$  are shown.

pair of counter-rotating roll modes or beneath hairpin packets, which sweep high-speed fluid downwards and eject low-speed fluid upwards, in the sense of instantaneous or conditional averaged flow fields (Adrian *et al.* 2000; Del Álamo *et al.* 2006; Adrian 2007; Hutchins & Marusic 2007*b*; Dennis & Nickels 2011; Lozano-Durán *et al.* 2012; Talluru *et al.* 2014; Wang *et al.* 2019*a*). Regarding  $u$  and  $v$ , which are strong within sweep or ejection motions, the signs remain the same at  $y_O^+$  and a near-wall position  $y^+$ . However, for the spanwise fluctuating velocity  $w$ , the sign probably changes along the wall-normal direction if keeping the same streamwise and spanwise location. This issue was already

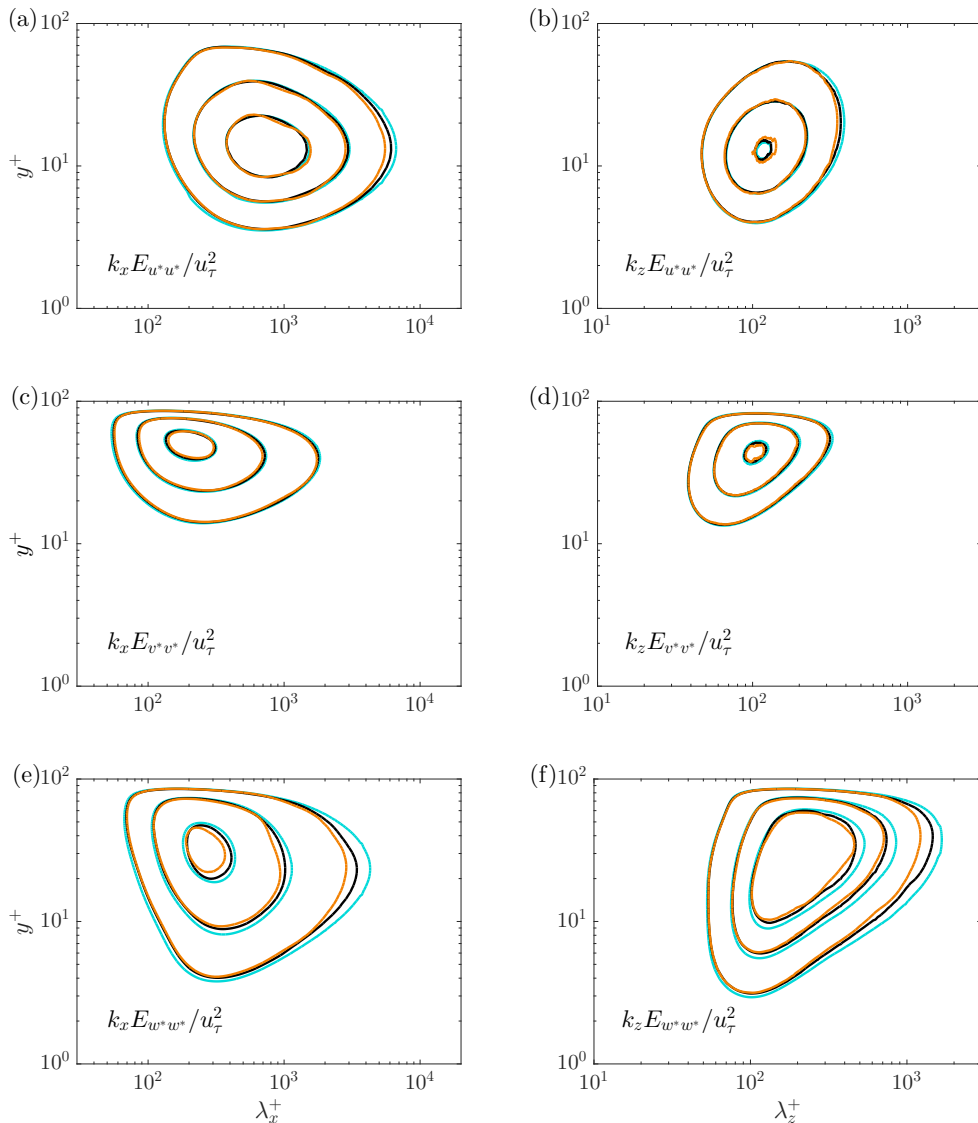


FIGURE 6. Pre-multiplied energy spectra of the three near-wall universal velocity components at  $Re_\tau = 1000, 2000$  and  $5200$ . The contour levels are (a)  $(0.6, 1.2, 1.8)$  for  $k_x E_{u^*u^*}/u_\tau^2$ ; (b)  $(1.2, 2.4, 3.6)$  for  $k_z E_{u^*u^*}/u_\tau^2$ ; (c)  $(0.1, 0.2, 0.3)$  for  $k_x E_{v^*v^*}/u_\tau^2$ ; (d)  $(0.17, 0.34, 0.51)$  for  $k_z E_{v^*v^*}/u_\tau^2$ ; (e)  $(0.2, 0.4, 0.6)$  for  $k_x E_{w^*w^*}/u_\tau^2$ ; (f)  $(0.2, 0.4, 0.6)$  for  $k_z E_{w^*w^*}/u_\tau^2$ .

addressed by Talluru *et al.* (2014), who finally proposed that “it is unlikely that a single-point input signal will be adequate to model the superposition component of the spanwise fluctuation”. Another possibility is the splattering effect (Agostini & Leschziner 2014; Agostini *et al.* 2016; Pan & Kwon 2018) or the dispersive motions (Hwang *et al.* 2016), since a portion of sweeping velocities is converted to spanwise motions, which is not contained in the superposition mechanism. Anyhow, although the extracted  $\langle w^{*2} \rangle$  is still a little  $Re_\tau$  dependent, we argue it is only marginal and acceptable, and should not be a substantial problem.

Moreover, we present evidence of the extracted universal near-wall motions in the

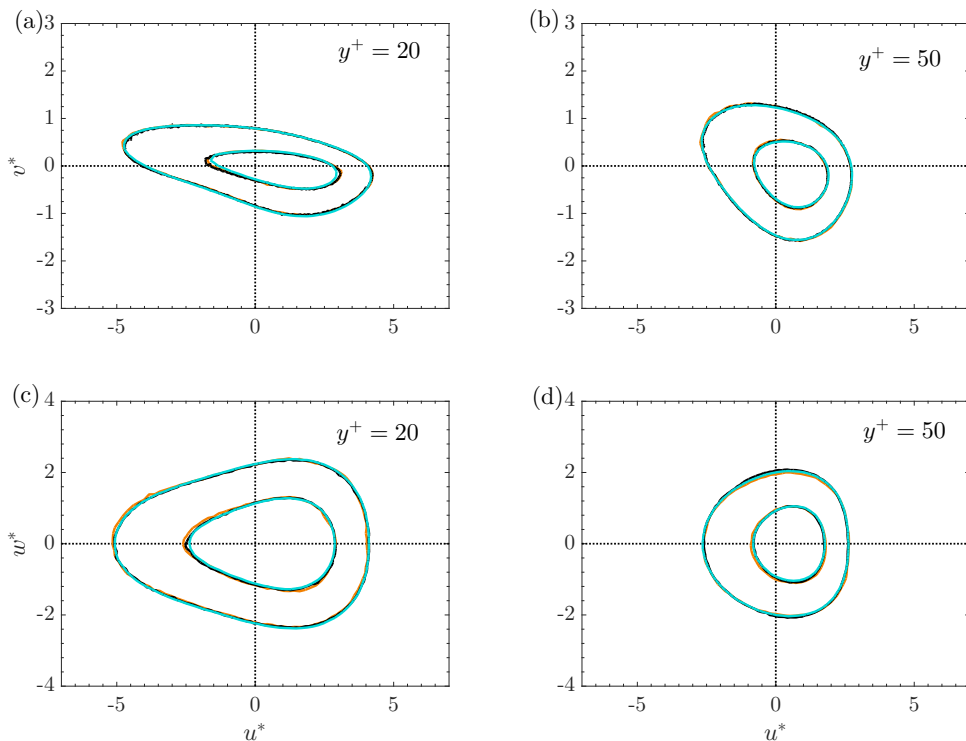


FIGURE 7. Joint p.d.f.s  $P(u^*, v^*)$  (a, b) and  $P(u^*, w^*)$  (c, d) at  $y^+ = 20$  (a, c) and  $y^+ = 50$  (b, d) in the fully developed turbulent channel flows at the Reynolds numbers  $Re_\tau = 1000 \sim 5200$ . The contour levels are (0.2, 0.6) normalized by the peak value of the p.d.f. at  $Re_\tau = 1000$  of the two heights.

scale space through pre-multiplied streamwise and spanwise energy spectra of all the three velocity components at the Reynolds numbers  $Re_\tau = 1000 \sim 5200$  with  $y_O^+ = 100$ , as shown in figure 6. It is clearly seen that the spectra of the extracted  $u^*$  and  $v^*$  collapse excellently at the different Reynolds numbers. The inner peaks of the streamwise and spanwise  $u^*$ -spectra locate at  $y^+ = 10 \sim 20$ ,  $\lambda_x^+ \sim O(10^3)$  and  $\lambda_z^+ \sim O(10^2)$ , which is well in accordance with experimental observations of near-wall streaks (Kline *et al.* 1967; Smith & Metzler 1983; Kim *et al.* 1987). For the wall-normal components  $v^*$ , the spectral peaks locate at  $y^+ \approx 50$ ,  $\lambda_x^+ = 200 \sim 300$  and  $\lambda_z^+ \approx 100$ . In accordance with the integrated spanwise velocity intensity  $\langle w^{*2} \rangle$ , it is also found there exists slight Reynolds number dependence in the pre-multiplied spectra of  $w^*$ , as displayed in figure 6 (e, f). The discrepancy is principally located at large wavelengths, i.e.,  $\lambda_x^+ > O(10^3)$  and  $\lambda_z^+ > 200 \sim 300$ . Here we claim again that this discrepancy is only marginal and could be neglected. The spectral peaks of  $w^*$  locate at similar wall-normal height and wavelengths with  $v^*$ , namely,  $y^+ = 30 \sim 40$ ,  $\lambda_x^+ = 200 \sim 300$  and  $\lambda_z^+ \approx 200$ . Therefore, the wall-normal positions of  $(v^*, w^*)$  spectral peaks are much higher than that of  $u^*$ , while their streamwise and spanwise wavelengths are much smaller, which is consistent with the characteristics of the near-wall inner spectral peaks before decomposition (figure 3). It is also noted that the  $u^*$  and  $w^*$  spectra can well penetrate into  $y^+ < 10$  while the  $v^*$  spectra are mainly located at  $y^+ > 10$ . This is due to the impermeable condition or the blocking effect of the wall-normal velocity at the wall (Perry & Chong 1982; Yang *et al.* 2018).

Furthermore, we present joint p.d.f.s  $P(u^*, v^*)$  and  $P(u^*, w^*)$  of the extracted near-wall universal velocities at the Reynolds number  $Re_\tau = 1000 \sim 5200$ , which is displayed in figure 7. The comparisons at the two wall-normal heights  $y^+ = 20$  and  $y^+ = 50$  exhibit remarkable coincidence of the joint p.d.f.s of the extracted universal velocity components at the three Reynolds numbers. The major axis of  $P(u^*, v^*)$  is inclined in the Q2-Q4 direction, indicating higher probabilities of the ejection and sweep motions. By comparing  $P(u^*, v^*)$  at the two heights, i.e. figure 7 (a) and (b), it can be seen that the inclination of the major axis is shallower at  $y^+ = 20$ , suggesting the ejecting or sweeping of the turbulent motions occurs at a smaller angle nearer the wall, similar to figure 4 (a, b). In addition, the joint p.d.f.  $P(u^*, w^*)$  is shown in figure 7 (c, d), which is symmetric about  $w^* = 0$  axis, also similar to figure 4 (c, d).

The above results demonstrate that truly universal near-wall turbulent motions that are independent of outer influences have been successfully extracted via the inner-outer interaction hypothesis, the extraction scheme (3.4-3.6) and the outer reference height  $y_O^+ = 100$ , in the Reynolds number range of  $Re_\tau = 1000 \sim 5200$ . In the study of Hwang (2013), the near-wall motions wider than  $\lambda_z^+ \approx 100$  were removed via the spanwise minimum flow unit. It was found that the filtered near-wall streamwise velocity fluctuations at  $y^+ \leq 40$  are well collapsed with the viscous scaling at the Reynolds numbers up to  $Re_\tau = 660$ . Yin *et al.* (2017) extended this approach to higher Reynolds numbers, i.e.,  $Re_\tau = 1000 \sim 4000$ , and obtained similar findings. We shortly comment here, that both Hwang (2013) and Yin *et al.* (2017) isolated healthy and Reynolds-number-invariant near-wall turbulent fluctuations at  $y^+ < \sim 50$  and  $\lambda_z^+ \leq 100$ , whereas the present methodology could finally extract universal near-wall turbulence in a higher wall-normal range ( $y^+ \leq 100$ ) and without spanwise wavelength restriction.

#### 4.1.2. Coherent structures

So far, Reynolds-number-invariant universal statistics of the decomposed small-scale near-wall motions have been thoroughly demonstrated, in the Reynolds number range of  $Re_\tau = 1000 \sim 5200$ . Now we turn to demonstrate the corresponding instantaneous flow snapshots and reveal the dominant coherent structures composing the universal near-wall flow.

Figure 8 displays  $x-z$  plane snapshots of the universal streamwise velocity at  $y^+ = 15$ , where the full streamwise velocity fluctuation intensity is approximately the maximum. It is seen that, as Reynolds number increases (i.e., figure 8 (a-c)), the general streaky features of the flows are quite similar, indicating that not only the statistics, but also the instantaneous fields of  $u^*$  exhibit good universal behavior. The  $v^*$  and  $w^*$  structures are also very similar at the three Reynolds numbers, which are not shown for saving the space.

It is well known that the near-wall region of a turbulent flow is comprised of various types of vortical structures (Robinson 1991; Adrian 2007; Stanislas 2017; Jiménez 2018; Lee & Jiang 2019). And the debate on the dominant near-wall vortical structures still remains elusive (Head & Bandyopadhyay 1981; Kim & Moin 1986; Jeong *et al.* 1997; Zhou *et al.* 1999; Schoppa & Hussain 2002; Sheng *et al.* 2009; Wu & Moin 2009; Yang & Pullin 2011; Schlatter *et al.* 2014; Eitel-Amor *et al.* 2015; Wang *et al.* 2015; Jodai & Elsinga 2016; Shekar & Graham 2018). Therefore it should be beneficial to present vortical structures of the decomposed near-wall velocity fields. Here the  $\lambda_{ci}$  criterion (Zhou *et al.* 1999) is employed for the vortex identification and visualization, which is defined as the imaginary part of the complex eigenvalue of velocity gradient tensor and usually referred to the local swirling strength. Vortical regions can be thus determined where the complex eigenvalues exist since the local flow is swirling. Figure 9 displays

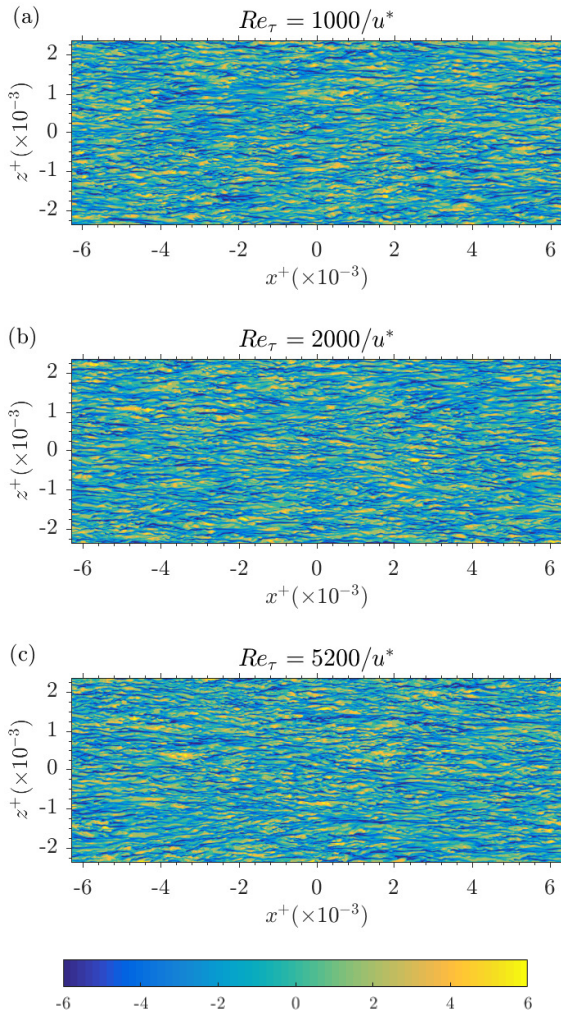


FIGURE 8. Plane snapshots at  $y^+ = 15$  of the near-wall universal streamwise velocity fields at (a)  $Re_\tau = 1000$ , (b)  $Re_\tau = 2000$ , and (c)  $Re_\tau = 5200$ .

instantaneous fields of  $\lambda_{ci,*}$  isosurfaces at the Reynolds numbers from 1000 to 5200. It is shown that quasi-streamwise vortices dominates the universal near-wall flow, however, there do exist signatures of hairpin vortex denoted by the red circles in the figure, despite the low number density.

In figure 10, we show Reynolds-number invariance of vortical statistics of the universal flow fields. The p.d.f.s of  $\lambda_{ci,*}$  at the three Reynolds numbers, i.e.,  $Re_\tau = 1000, 2000$  and  $5200$ , are plotted in figure 10 (a), which demonstrate excellent agreement among the three distributions. Meanwhile, the wall-normal variation of the most probable value of  $\lambda_{ci,*}$  is represented by the black dotted line, the maximum of which is located around  $y^+ = 25$ . Furthermore, figure 10 (b) exhibit the mean swirling strength profiles. It is seen that, the mean swirling strength increases first and then decreases with  $y^+$ , and the maximum also appears at  $y^+ = 25$ . Excellent Reynolds-number invariance is observed. An approximately linear variation of the mean swirling strength  $\langle \lambda_{ci,*} \rangle$  with  $y^+$  in the range of  $y^+ \approx 30 \sim 75$  is also denoted in the figure. Since the swirling strength is defined

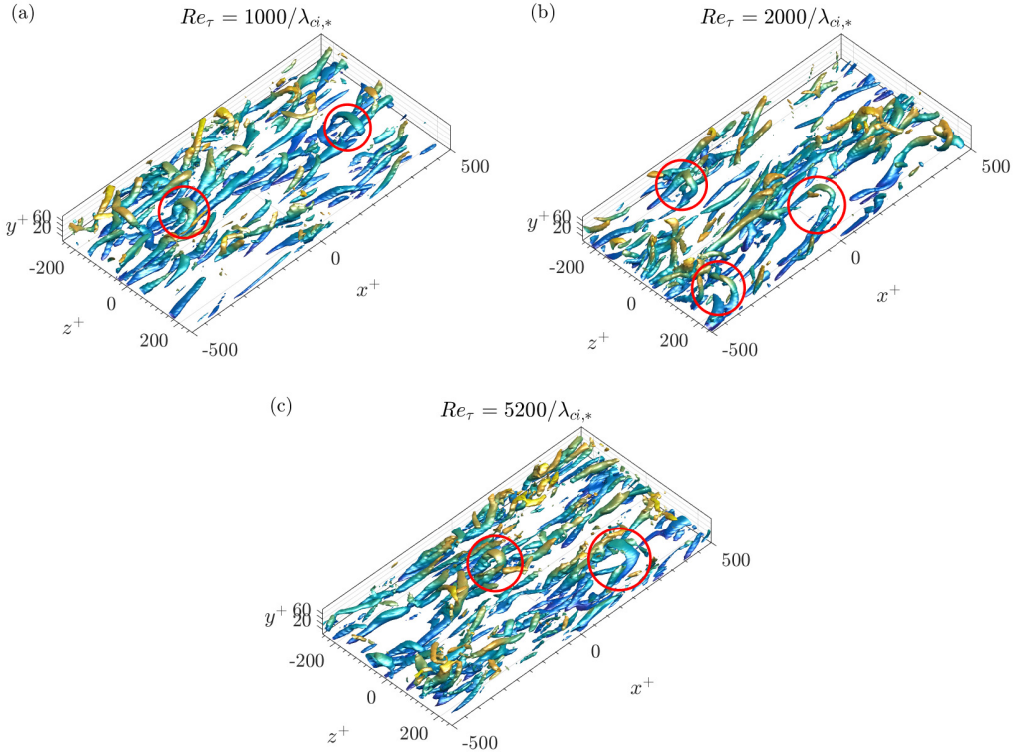


FIGURE 9. Vortex structures from instantaneous universal velocity fields at  $Re_\tau = 1000, 2000, 5200$ , identified by  $\lambda_{ci,*} = 0.10$ .

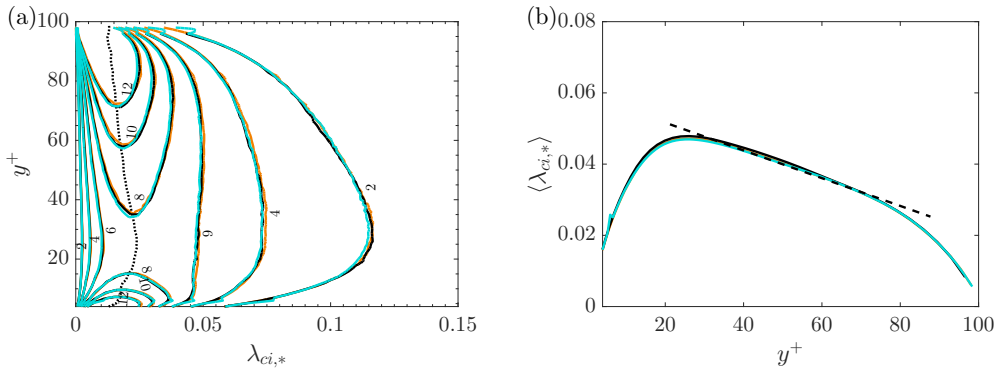


FIGURE 10. P.d.f.s of  $\lambda_{ci,*}$  (a) and mean swirling strength  $\langle \lambda_{ci,*} \rangle$  (b) as functions of  $y^+$  at  $Re_\tau = 1000, 2000$  and  $5200$ .

in terms of velocity gradient, it is of higher order than velocity itself, and the comparison here further strengthens the reliability of the current extraction scheme for the universal velocity field.

Besides swirling strength  $\lambda_{ci}$ , vortex orientation is another important aspect for the characterization of vortical structures. Zhou *et al.* (1999) suggested that local swirling flow will be stretched or compressed along the direction of the real eigenvector  $\Lambda_r$  of the velocity gradient tensor. Gao *et al.* (2011) employed  $\Lambda_r$  to identify the local vortex



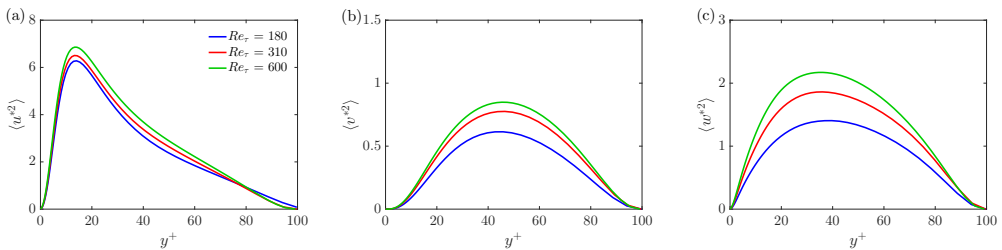


FIGURE 12. Turbulence intensities of the extracted small-scale near-wall fluctuating velocity components at  $Re_\tau = 180, 310$  and  $600$ : (a) streamwise velocity, (b) wall-normal velocity, and (c) spanwise velocity.

and  $y^+ \approx 30 \sim 40$ , respectively. Therefore, the extracted  $\langle u^{*2} \rangle$ ,  $\langle v^{*2} \rangle$  and  $\langle w^{*2} \rangle$  are not universal, instead they show definite Reynolds number dependence. And we will denote it as the low Reynolds number effect hereafter, which should not be confounded with that in the literature (Antonia *et al.* 1992; Antonia & Kim 1994), since the latter was declared for the undecomposed turbulent flows.

Furthermore, similar to figure 6, we show the one-dimensional streamwise and spanwise pre-multiplied energy spectra of the three small-scale velocity components at the low Reynolds numbers in figure 13, with the viscous-scaled wavelength ( $\lambda_x^+$  or  $\lambda_z^+$ ) and the wall-normal height ( $y^+$ ). For the contour level, we try to keep consistent with figure 6, but for clarity, only two levels between zero and the peak values are shown. As displayed in figure 13 (a,b), the near-wall spectral peaks of the streamwise and spanwise pre-multiplied spectra locate at  $y^+ = 10 \sim 20$  with  $\lambda_x^+ \sim O(10^3)$  and  $\lambda_z^+ \sim O(10^2)$ , which are similar with those in figure 3 and figure 6. However, it may not be claimed with confidence that the spectral contours are perfectly scaled by viscous units. In fact, figure 13 (a) shows that the streamwise wavelength of the inner peak is slightly larger at lower Reynolds numbers, which is consistent with our previous simulations at much lower Reynolds numbers (Hu & Zheng 2018). Meanwhile, the spanwise wavelength of the inner peak is larger at higher Reynolds number, see figure 13 (b). This may indicate that as Reynolds number increases, the near-wall small-scale  $u^*$  structures tend to be shorter and wider, in the low Reynolds number regime. Moreover, in figure 13 (c-f), the streamwise and spanwise pre-multiplied energy spectra of  $v^*$  and  $w^*$  are presented, in which the wall-normal locations of the inner spectral peaks are also consistent with the undecomposed ones, as in figure 3 (c-f), say  $y^+ = 30 \sim 70$ . Compared to the  $u^*$ -spectra, the  $v^*$ - and  $w^*$ -spectra exhibit much stronger Reynolds number dependence. Particularly, as Reynolds number increases, the spectral energy increases accordingly, resulting in stronger integrated  $\langle v^{*2} \rangle$  and  $\langle w^{*2} \rangle$ , as shown in figure 12 (b) and (c). Since the spanwise and wall-normal velocity components are closely related to vortical structures, it may imply that the strength of near-wall small-scale quasi-streamwise vortices increases with Reynolds number in the low  $Re_\tau$  regime ( $Re_\tau < 1000$ ), and can reach a fully-developed asymptotic status once  $Re_\tau \geq 1000$ . It should be mentioned that Antonia & Kim (1994) also attributed the low-Reynolds-number effect to an increase in strength of the quasi-streamwise vortices in the buffer layer, other than the average diameter or average location.

To demonstrate the low Reynolds number effect on the instantaneous coherent structures, figure 14 shows the plane snapshots at  $y^+ = 15$  of instantaneous  $u^*$  fields at  $Re_\tau = 180, 310$  and  $600$ . From this figure, it can be generally seen that the spanwise width of the near-wall streaks increases with Reynolds number. For the streamwise length of the streaks, it is much more difficult to inspect a distinction visually. However, through spectral analysis, we know that the  $u^*$  structures should be shortened at higher Reynolds

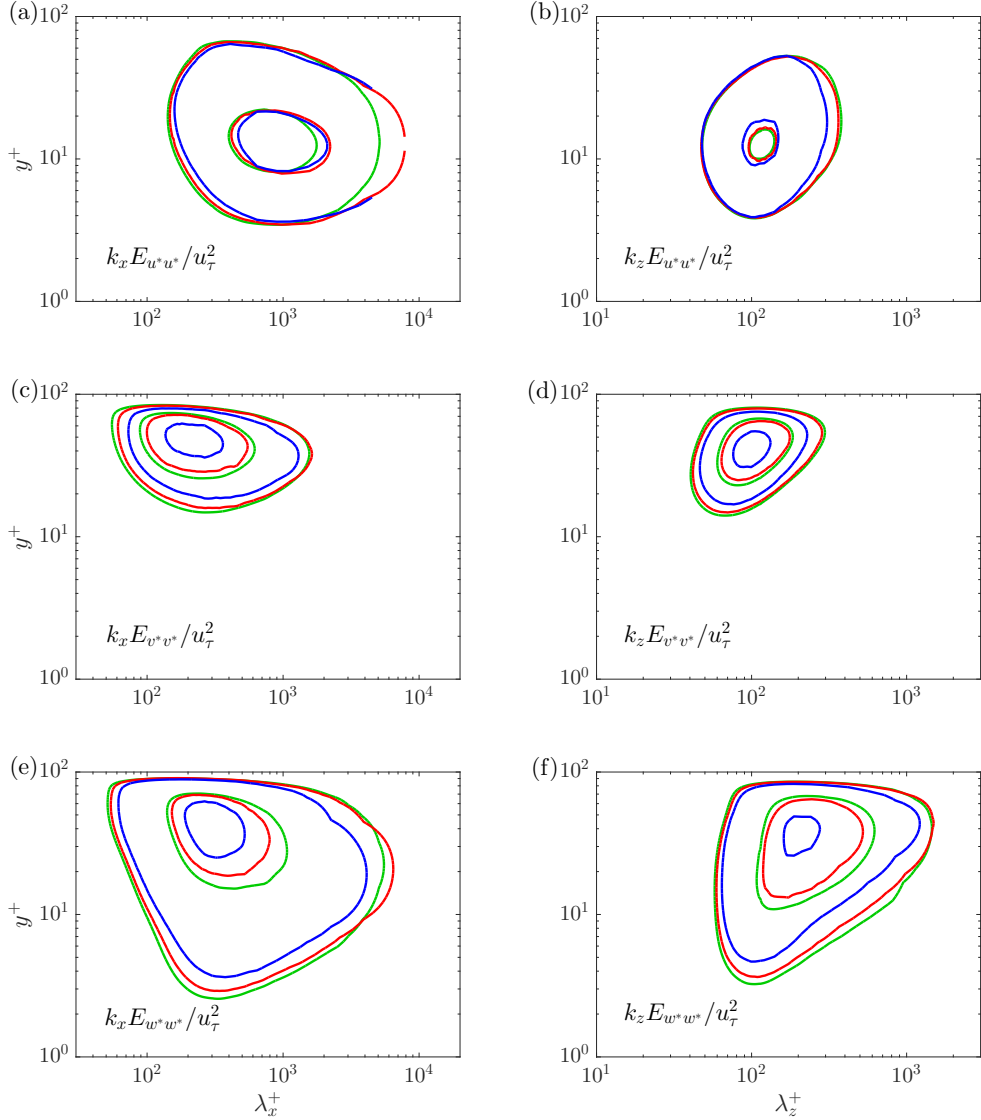


FIGURE 13. Pre-multiplied energy spectra of the three near-wall small-scale velocity components at  $Re_\tau = 180, 310$  and  $600$ . The contour levels are equally spaced from zero to the corresponding peak values, which are (a)  $(0.6, 1.8)$  for  $k_x E_{u^* u^*} / u_\tau^2$ ; (b)  $(1.2, 3.6)$  for  $k_z E_{u^* u^*} / u_\tau^2$ ; (c)  $(0.1, 0.2)$  for  $k_x E_{v^* v^*} / u_\tau^2$ ; (d)  $(0.17, 0.34)$  for  $k_z E_{v^* v^*} / u_\tau^2$ ; (e)  $(0.2, 0.6)$  for  $k_x E_{w^* w^*} / u_\tau^2$ ; (f)  $(0.2, 0.6)$  for  $k_z E_{w^* w^*} / u_\tau^2$ .

number if  $Re_\tau < 1000$ . In addition, figure 15 displays instantaneous vortical fields with  $\lambda_{ci,*} = 0.15$  at the three low Reynolds numbers. It clearly shows that quasi-streamwise vortices populate in the near wall region, and their lengths are around  $100 \sim 200$  viscous units, which is consistent with many previous results (Head & Bandyopadhyay 1981; Jeong *et al.* 1997; Hwang 2013; Wang *et al.* 2019a). Furthermore, one distinctive feature in the figure is the increasing trend of vortex population with Reynolds number. However, it does not necessarily indicate more vortices at higher Reynolds number, but vortices are getting stronger, as more intense regions of  $\lambda_{ci,*} > 0.15$  are detected. Therefore, per

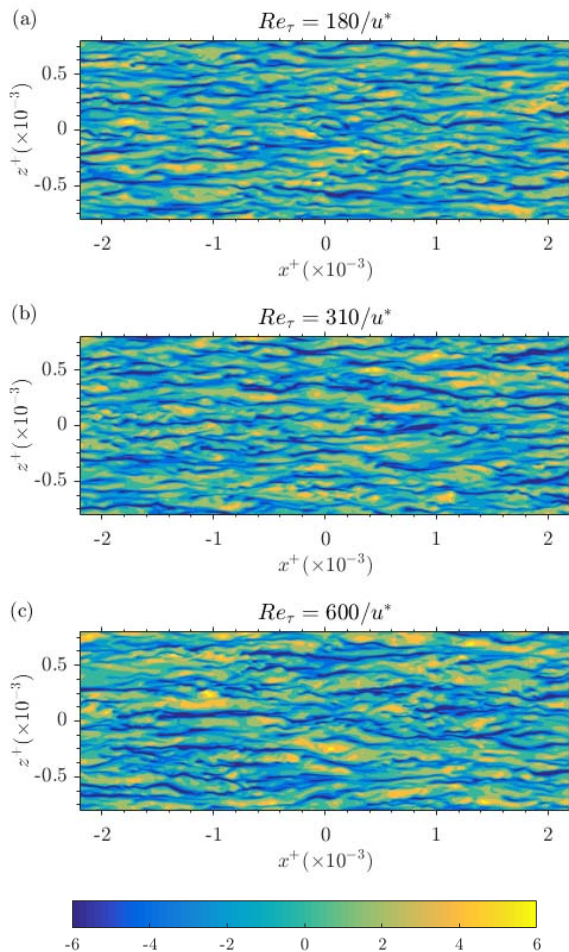


FIGURE 14. Plane snapshots at  $y^+ = 15$  of the near-wall small-scale streamwise velocity fields at (a)  $Re_\tau=180$ , (b)  $Re_\tau =310$ , and (c)  $Re_\tau =600$ .

the instantaneous flow fields, we revealed that near-wall small-scale streaks tend to be shorter and wider, while vortical structures are getting stronger with Reynolds number at  $Re_\tau < 1000$ .

Finally, we illustrate the low-Reynolds-number effect on the swirling strength statistics. The p.d.f. distributions of  $\lambda_{ci,*}$  at  $Re_\tau = 180, 310$  and  $600$  in the near-wall region are compared in figure 16 (a). The shapes of the p.d.f.s at the different Reynolds numbers are generally similar. However, it can be clearly seen that, as Reynolds number increases, the probability of large swirling strength gradually becomes higher, indicating stronger vortical strength at higher  $Re_\tau$ . Besides, figure 16 (b) demonstrates the mean swirling strength profiles at the three low Reynolds numbers. The swirling strength increases first then decreases with  $y^+$ , and the maximum value appears at  $y^+ \approx 25$ , which is similar to the higher Reynolds number cases, as in figure 10 (b). However, the absolute value of  $\lambda_{ci,*}$  is found to increase with  $Re_\tau$  and be consistent with the p.d.f. result. Moreover, the linear relationship also exists and almost has an identical slope from  $Re_\tau = 180$  to  $5200$  in the range of  $y^+ = 30 \sim 75$ . In addition, the mean inclination and the corresponding

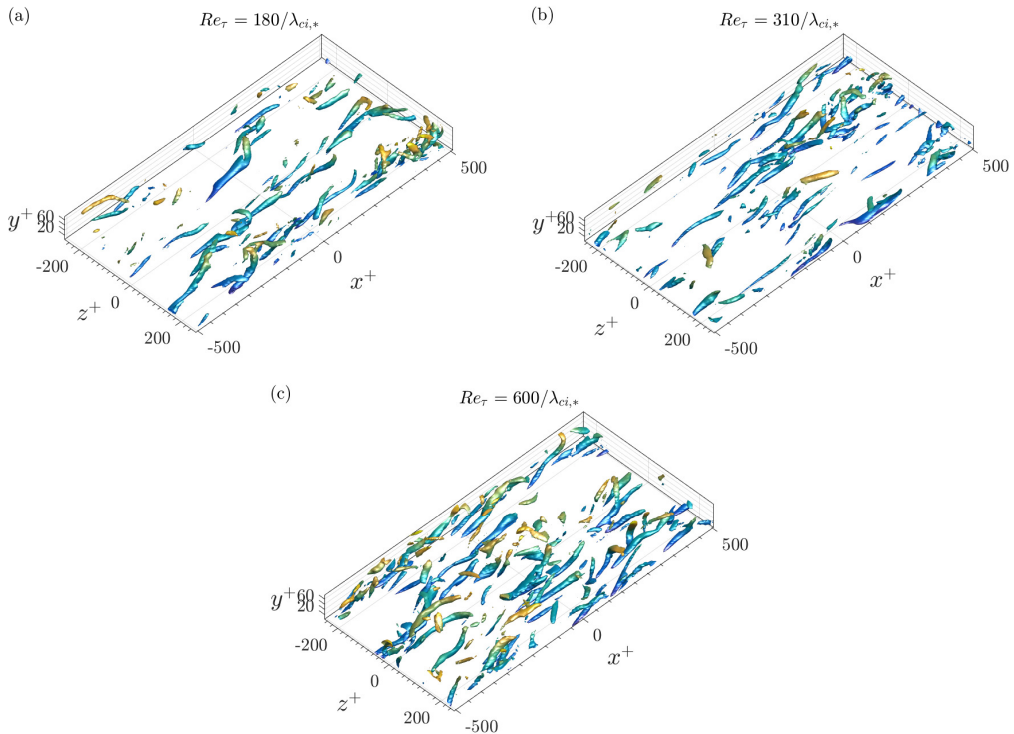


FIGURE 15. Vortex structures from the instantaneous universal velocity fields at (a)  $Re_\tau = 180$ , (b)  $Re_\tau = 310$ , and (c)  $Re_\tau = 600$ , identified by  $\lambda_{ci,*} = 0.10$ .

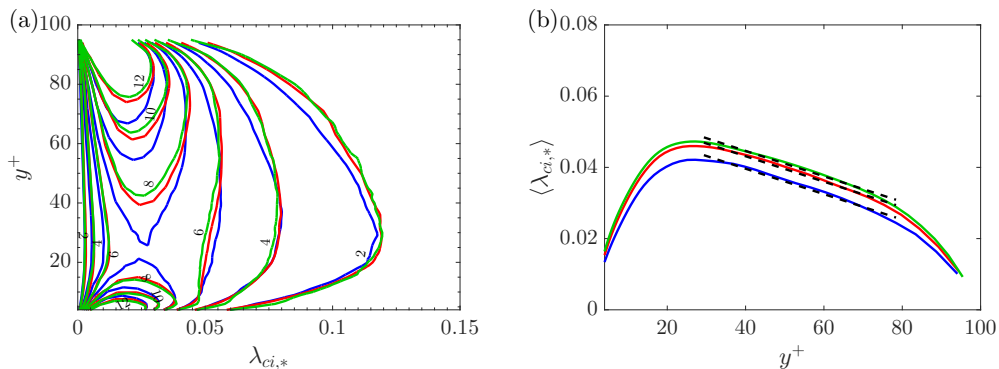


FIGURE 16. P.d.f.s of  $\lambda_{ci,*}$  (a) and mean swirling strength  $\langle \lambda_{ci,*} \rangle$  (b) as functions of  $y^+$  at  $Re_\tau = 180, 310$  and  $600$ .

p.d.f. of the near-wall small-scale vortex structures are found to be basically independent of Reynolds number, which are not shown here for saving space.

In summary, we have applied the decomposition scheme (3.4-3.6) to the low-Reynolds-number turbulent channels at  $Re_\tau = 180 \sim 600$ , and the extracted near-wall small-scale velocity fields ( $u^*$ ,  $v^*$  and  $w^*$ ) are discovered to be Reynolds number dependent. The main mechanism may be the strengthening of the near-wall quasi-streamwise vortical structures. And it will induce the augments of the velocity fluctuations, as well as the widening and shortening of the near-wall streaks.

## 4.3. Characteristics of the outer footprints and inter-scale interactions

In this part, we present the characteristics of the near-wall footprints of outer turbulent motions, i.e.,  $(u_L, v_L, w_L)$ , also known as the superposition effect (Hutchins & Marusic 2007b; Marusic *et al.* 2010a; Mathis *et al.* 2011), as well as their interactions with the near-wall small-scale motions, which is quantified by the amplitude modulation of large scales to small scales.

First, we explore the instantaneous  $u_L$  fields, representing the "footprints" of outer streamwise fluctuating velocity in the near-wall region, which is simply obtained by invoking (3.2), as shown in figure 17. As we can see, the representative  $x - z$  plane snapshots of  $u_L$  fields at  $y^+ = 15$  with  $Re_\tau = 180 \sim 5200$  are directly compared, in which the islands surrounded by the solid lines indicate the areas of intensive  $u_L$  fluctuations with a level  $u_L^+ = \pm 1.5$ . It is noted that we only take  $x^+ = -2.2 \times 10^3 \sim 2.2 \times 10^3$  and  $z^+ = -8 \times 10^2 \sim 8 \times 10^2$  at  $Re_\tau = 180, 310$  and  $600$ , while  $x^+ = -6.25 \times 10^4 \sim 6.25 \times 10^4$  and  $z^+ = -2.3 \times 10^3 \sim 2.3 \times 10^3$ , since the viscous-scaled domain size is smaller at low Reynolds numbers. From figure 17 (a-f), it could be seen that, as Reynolds number increases, the viscous-scaled length and width of the intensive velocity fluctuation regions progressively increase in general. The number of the identified regions also increases with  $Re_\tau$ . At the Reynolds numbers of  $Re_\tau = 180$ , we can hardly find an intensive velocity fluctuation region in the snapshot. While at  $Re_\tau = 5200$ , there exists a large number of intensive  $u_L$  regions, some of which even exceed the shown spatial range of the snapshot.

In order to further quantify the contributions of  $(u_L, v_L, w_L)$  to the total turbulent kinetic energy (TKE) in the near-wall region, here we define  $\pi_i = \langle u_{i,L}^2 \rangle / \langle u_i^2 \rangle$  ( $i = x, y, z$  corresponding to the three Cartesian directions), as the contribution ratio of the outer footprint TKE to the total TKE. Figure 18 (a,c,e) shows the contribution ratio  $\pi_i$  of all the three velocity components at the different Reynolds numbers. It is seen that  $\pi_x$ ,  $\pi_y$  and  $\pi_z$  all increase with  $y^+$ , demonstrating more TKE contributions of the outer footprints away from the wall, and finally reach 1.0 at  $y^+ = 100$  due to  $y_O^+ = 100$  in the extraction scheme (3.2). The horizontal dotted line in figure 18 (a,c,e) marks the 50% TKE contribution from the outer footprints, and the shaded region illustrates the wall-normal range of  $\pi_i = 0.5$  at  $Re_\tau = 180 \sim 5200$ . We can see that the TKE contributions of outer footprint in the three directions are stronger at higher Reynolds number. Taking  $\pi_x$  for example, the wall-normal height of  $\pi_x = 0.5$  is  $y^+ \approx 78$  at  $Re_\tau = 180$  while  $y^+ \approx 48$  at  $Re_\tau = 5200$ , indicating a growing contribution of  $\langle u_L^2 \rangle$  to  $\langle u^2 \rangle$  as  $Re_\tau$  increases. Moreover, compared to the wall-normal component  $\pi_y$ ,  $\pi_x$  and  $\pi_z$  exhibit much stronger Reynolds number dependence in the near-wall region, e.g.,  $\pi_x$  is even as high as about 0.2 at the wall if  $Re_\tau = 5200$ . This is consistent with the attached eddy hypothesis of Townsend (1976), that the near-wall region could feel wall-parallel motions due to the attached eddies that reside above that point. Here we take a further look at the wall-normal contribution ratio  $\pi_y$ , which is shown in figure 18 (c). Notable Reynolds number invariant or universal behavior of  $\pi_y$  is observed at  $Re_\tau \geq 600$ , while it may not necessarily imply  $\langle v_L^2 \rangle^+$  is Reynolds number invariant, since the total wall-normal TKE  $\langle v^2 \rangle^+$  indeed shows  $Re_\tau$  dependence.

The wall-normal variations of the coefficients  $\langle \gamma_{uu}^2 \rangle$ ,  $\langle \gamma_{uv}^2 \rangle$  and  $\langle \gamma_{uw}^2 \rangle$ , whose definitions can be deduced from (3-3) as the ratio between the universal and the small-scale velocity variances  $\langle u_i^{*2} \rangle / \langle u_{i,S}^2 \rangle$ , are displayed in figure 18 (b,d,f). Considering the fact that  $u_i^*$  is obtained from the demodulation operation of  $u_{i,S}$ , these parameters could be utilized for quantifying the amplitude modulation effect in an average sense. It is seen from figure 18 (b,d,f) that the coefficients are obviously very close to 1.0, the maximum deviation of which is less than 5%. Therefore, the variances of  $u_i^*$  and  $u_{i,S}$  are almost identical, and

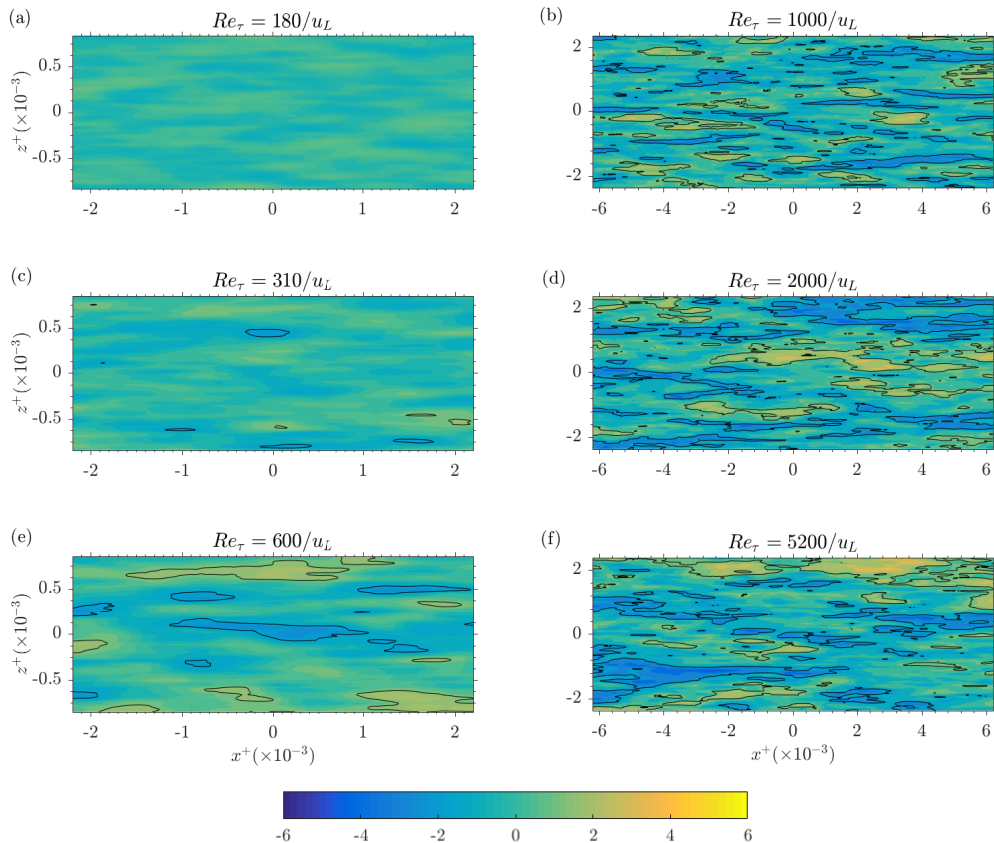


FIGURE 17. Plane snapshots of the outer footprints  $u_L^+$  at  $y^+ = 15$ . The Reynolds number is indicated at the top of each subfigure. The solid lines indicate the contour level of  $u_L^+ = \pm 1.5$ .

one may arrive the point that the amplitude modulation effect is negligible in the average sense, at least in the Reynolds number range of the current study.

We further scrutinize the spectral energy distributions of the outer footprints in the near-wall region. The streamwise pre-multiplied energy spectra of all the three velocity components, against the inner- and outer-scaled wavelength ( $\lambda_x^+$  and  $\lambda_x/\delta$ ), are given in figure 19 (a,b). In figure 19 (a), it is shown that the TKE spectral distribution of  $u_L$  seems to obey the viscous scaling very well in the range of  $\lambda_x^+ < 6000$  at  $Re_\tau \geq 1000$ . With the outer scaling, we can see that the  $u_L$  spectra collapse with each other very well for  $\lambda_x/\delta > 6$  at  $Re_\tau \geq 1000$ , see figure 19 (b). Furthermore, the pre-multiplied energy spectra of the wall-normal velocity footprints  $v_L$  are displayed in figure 19 (c,d) with the viscous and outer scaling, respectively. It is seen that, clear Reynolds number dependence of the  $v_L$  spectra exists with the outer scaling, see figure 19 (d). In contrast, excellent collapse is found with the viscous scaling at  $\lambda_x^+ < 1000$  and  $Re_\tau \leq 1000$ , as displayed in figure 19 (c). The pre-multiplied spectra of the spanwise velocity footprints  $w_L$  are shown in figure 19 (e,f). In the wavelength region of  $\lambda_x^+ \leq 600$  and  $Re_\tau \leq 1000$ , it can be clearly seen that the spectra are well collapsed with the viscous-scaled wavelength, see figure 19 (e). However, from figure 19 (f), we may not confirm a collapse of the  $w_L$  spectra with the outer-scaled wavelength, as good as the streamwise one. The excellent collapse of  $u_L$ ,  $v_L$  and  $w_L$  spectra with the viscous-scaled wavelength in the small-scale regimes, may

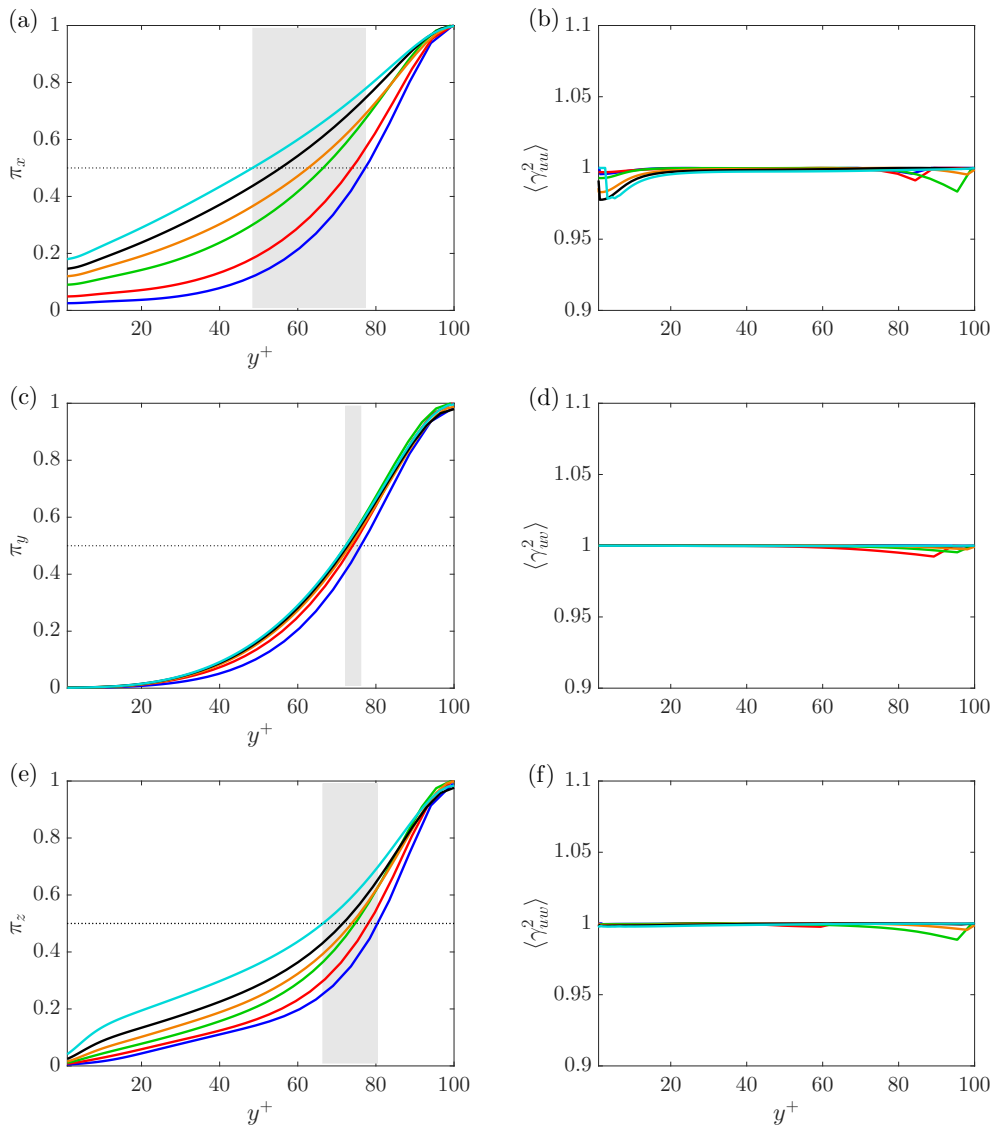


FIGURE 18. TKE contribution ratio  $\pi_i$  (a,c,e) and the modulation ratio  $\langle \gamma^2 \rangle$  between  $\langle u_i^{*2} \rangle$  and  $\langle u_{i,S}^2 \rangle$  (b,d,f) of the three velocity components in the near-wall region.

imply possible relations of the small-scale parts of the outer footprints (as well as the corresponding outer motions) with the viscous-dominated near-wall turbulence.

Next, we move on to analyze the contribution of the outer footprints on the swirling strength in the near-wall turbulence. Figure 20 displays the wall-normal variations of the p.d.f.s of swirling strength  $\lambda_{ci}$  in the near-wall region at  $Re_\tau = 1000$ , including those from the full and the decomposed velocity fields. Figure 20 (a) compares the p.d.f.s of  $\lambda_{ci}$  from the original, the small-scale and the universal velocity fields, namely,  $\lambda_{ci}$ ,  $\lambda_{ci,S}$  and  $\lambda_{ci,*}$ . First, it is clearly seen that the p.d.f.s of  $\lambda_{ci,*}$  and  $\lambda_{ci,S}$  coincide with each other very well, which is consistent with the earlier results that the statistics of  $u_i^*$  and  $u_{i,S}$  are almost identical. Moreover, it is interesting to note that the p.d.f. distribution of  $\lambda_{ci}$  from the full velocities below the buffer layer ( $y^+ < 30$ ) can be well approximated

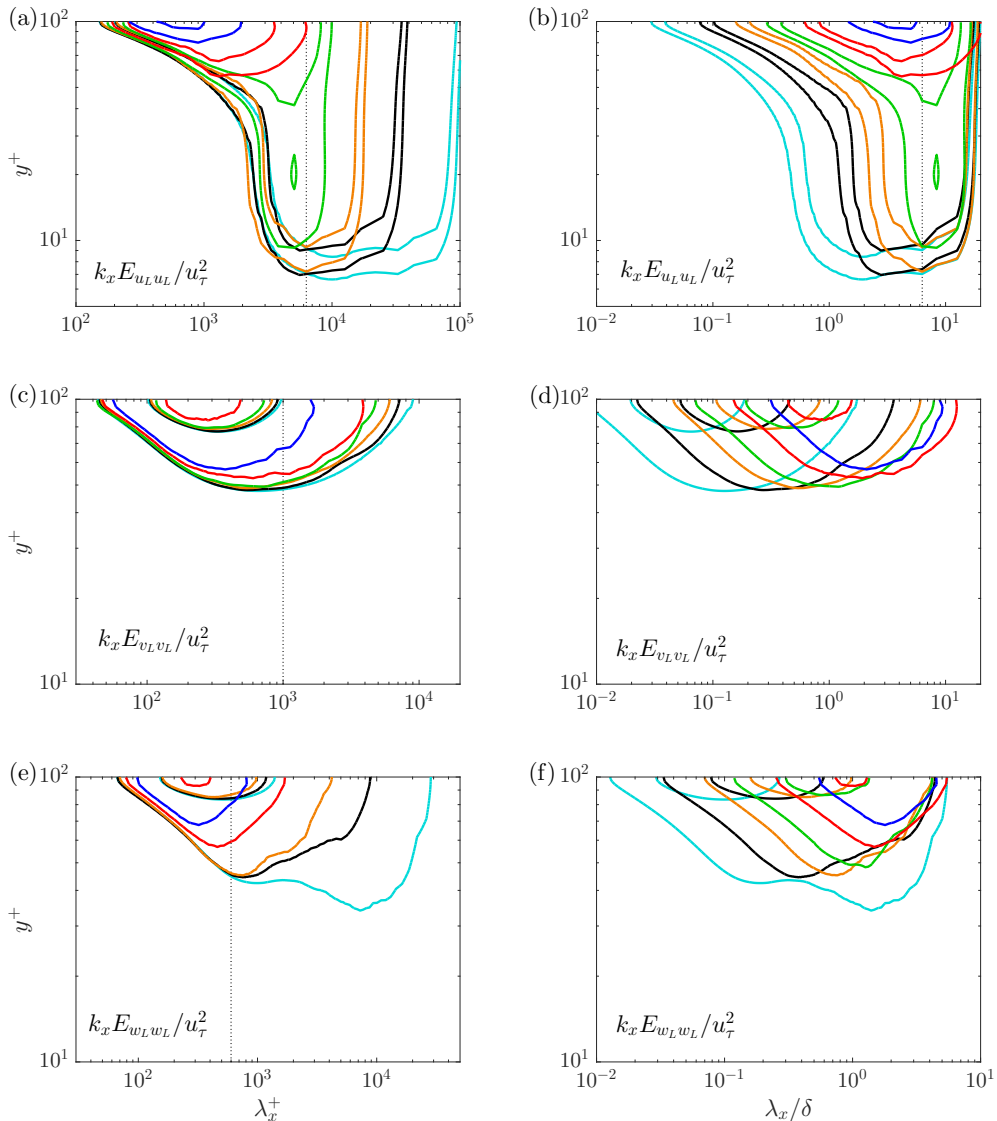


FIGURE 19. Streamwise pre-multiplied energy spectra of the outer footprint velocity components ( $u_L, v_L, w_L$ ) with the viscous-scaled wavelength  $\lambda_x^+$  (a,c,e) and the outer-scaled wavelength  $\lambda_x/\delta$  (b,d,f).

by that of  $\lambda_{ci,S}$  or  $\lambda_{ci,*}$ . Above the buffer layer, i.e.,  $y^+ > 30$ , the swirling strength of the small-scale or universal flow tends to be smaller than that in the full field. Figure 20 (b) shows the p.d.f. of  $\lambda_{ci,L}$  in comparison with that of  $\lambda_{ci}$ . As wall-normal height increases, the p.d.f. distribution of  $\lambda_{ci,L}$  is wider that implies higher possibility of larger swirling strength. Therefore, we can state that the vortical structures of the outer footprints are only apparent above the buffer layer. In other words, the vortical structures in the buffer layer are principally generated by the near-wall small-scale motions.

At last, we demonstrate the Reynolds-number effect on the swirling strength statistics of outer footprint fields. The p.d.f. distributions of  $\lambda_{ci,L}$  at the Reynolds numbers from 180 to 5200 in the near-wall region are compared in figure 21 (a). The contours

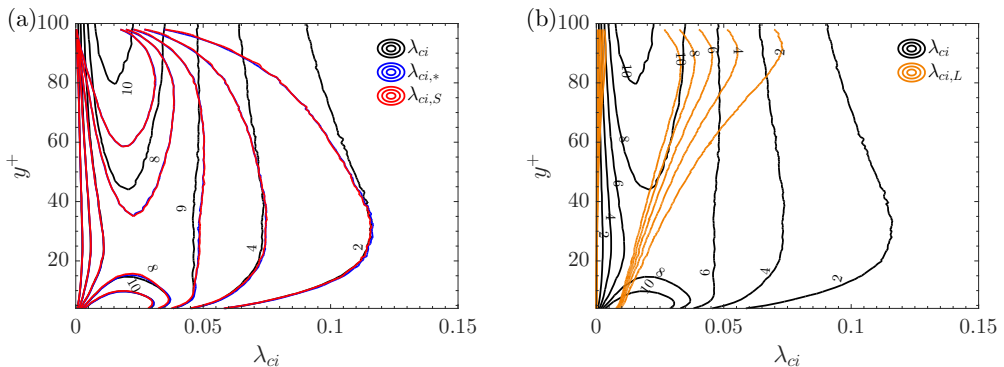


FIGURE 20. Comparison of the p.d.f.s of the swirling strength calculated from the full velocity field ( $\lambda_{ci}$ ), the large-scale outer footprint velocity field ( $\lambda_{ci,L}$ ), the small-scale velocity field ( $\lambda_{ci,S}$ ) or the universal velocity field ( $\lambda_{ci,*}$ ).

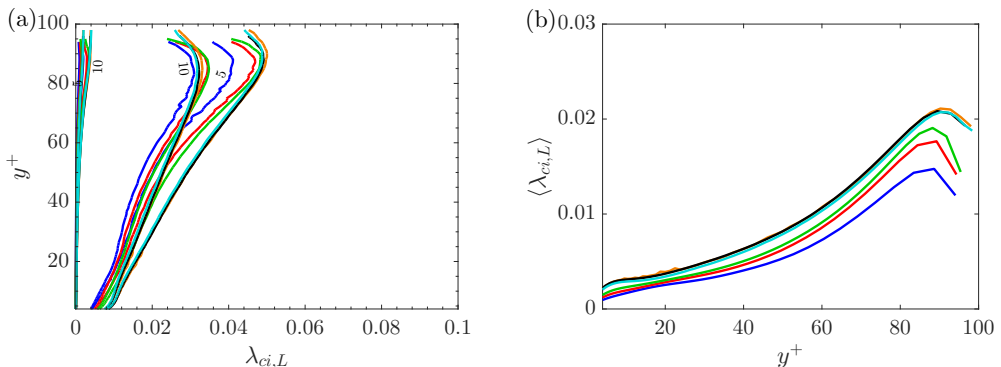


FIGURE 21. P.d.f.s (a) and mean profiles (b) of  $\lambda_{ci,L}$  as functions of  $y^+$  at the Reynolds numbers from 180 to 5200.

of the p.d.f.s exhibit excellent collapse at the Reynolds numbers of 1000, 2000 and 5200. However, the swirling strengths at lower Reynolds numbers show definite  $Re_\tau$  dependence, and decreases as Reynolds number decreases. Meanwhile, figure 21 (b) displays the mean swirling strength profiles at different Reynolds numbers. It can be seen that, the mean swirling strength  $\langle \lambda_{ci,L} \rangle$  is generally larger at higher  $y^+$ , while only decays at about  $y^+ > 90$  possibly due to the decrease of the gradient of  $u_{i,L}$  near  $y^+ = 100$ . At the three high Reynolds numbers, i.e.,  $Re_\tau = 1000, 2000$  and  $5200$ , the  $\langle \lambda_{ci,L} \rangle$  profiles collapse very well, but not the case at lower Reynolds numbers, which is consistent with figure 21 (a). By connecting with the results of the outer footprint velocities, it may suggest that the outer imprint vortical structures are probably generated by the viscous-scaled small-scale parts of  $u_{i,L}$ . In other words, the large-scale parts of  $u_{i,L}$  are passive while not active vortical structures.

## 5. Concluding remarks

In this work, we present a decomposition methodology of three-dimensional turbulence velocities into small-scale and large-scale components in the near-wall region at  $y^+ < 100$ . The method is principally based on the PIO model of Marusic *et al.* (2010a) and Mathis *et al.* (2011). However, a significant difference is that we use  $y_0^+ = 100$  instead of  $y_0^+ \sim$

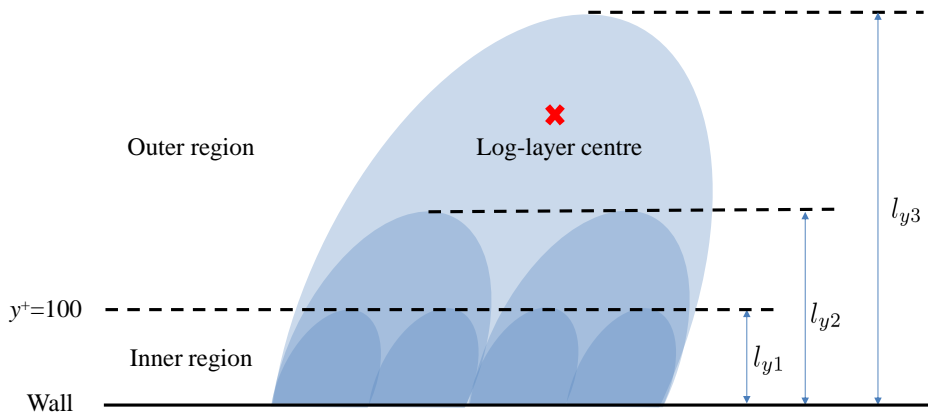


FIGURE 22. Schematic illustration of a hierarchical structure of attached eddies with three levels.

$\sqrt{Re_\tau}$  as the reference height for evaluating outer footprints. Reynolds-number-invariant universal small-scale turbulent motions are then extracted at  $1000 \leq Re_\tau \leq 5200$  with plenty of evidence, including the integrated intensities, the spectra and the p.d.f.s of fluctuating velocities in the three directions, the instantaneous coherent structures and characteristics of swirling quantities. The reason can be simply attributed to that the eddies with size of  $100 < l_y^+ < \sqrt{Re_\tau}$  should also be responsible for near-wall footprints and need to be incorporated, and  $y^+ \approx 100$  can be regarded as the 'critical' dividing height of inner and outer regions in the context of wall-bounded turbulence fluctuations. A recent experimental investigation in open channel flows also support it (Duan *et al.* 2020).

This can be further elucidated by the properties of the attached eddies and detached eddies (Perry & Marusic 1995; Baars & Marusic 2020a; Hu *et al.* 2020) that both have coherence with the wall. The detached eddies are longer than the attached eddies and peaked at the centre of the logarithmic layer approximately. This is why previous studies commonly used  $y_O^+ \sim \sqrt{Re_\tau}$  where the outer spectral peak resides (Mathis *et al.* 2011; Baars *et al.* 2016). However, the attached eddies are more populated near the wall and lead to the logarithmic decay of  $\langle u^2 \rangle^+$ . As illustrated in figure 22, if we use  $y_O^+ \sim \sqrt{Re_\tau}$ , only the contribution of the third-level attached eddies with  $l_{y3}$  in size is included. In order to take into account smaller eddies, it is required to let  $y_O^+ = l_{y1}^+$ , i.e., the size of the smallest attached eddies. According to the present finding, it is suggested that  $l_{y1}^+ = y_O^+ \approx 100$ , which is consistent with previous conjecture that the smallest attached eddies should be on the order of 100 viscous units in height (Perry & Chong 1982).

At lower Reynolds numbers of  $Re_\tau \leq 600$ , we find that the extracted small-scale velocity and swirling-strength statistics can not be scaled by the viscous units. The intensities of these turbulence quantities increase with Reynolds number, showing a developing trend of near-wall small-scale turbulence. After examining the vortical structures, it is revealed that the overall swirling strength of the small-scale motions is enhanced at larger  $Re_\tau$ , which is consistent with the vortex strengthening mechanism (Wei & Willmarth 1989; Antonia *et al.* 1992; Antonia & Kim 1994). We would like to note that the low-Reynolds-

number effect is also consistent with our previous simulations at lower Reynolds numbers (Hu & Zheng 2018). Although a wide range of viscous scaling is not established at low Reynolds numbers, it is still speculated that turbulent outer motions may emerge at a quite small Reynolds number as  $Re_\tau \approx 100$ , since  $y^+ > 100$  is suggested as the outer region here.

Finally, we address the characteristics of the outer footprints and inter-scale interactions. Both the viscous-scaled intensities and length scales of the outer footprints increase with Reynolds number. Interestingly, it is also discovered that the small-scale part of the outer footprints can be well scaled by the viscous units, as well as the vortical statistics, indicating possible relations with the near-wall small-scale motions. Another finding is that in average, the statistics of  $(u^*, v^*, w^*)$  are almost identical to those of  $(u_S^+, v_S^+, w_S^+)$ , implying that the average effect of amplitude modulation could be negligible. However, we do not deny that within positive/negative fluctuating regions of the outer footprints, the small-scale intensities would be amplified/depressed, which will be analyzed in the future.

## Acknowledgement

Financial supports by grants from the National Natural Science Foundation of China (11490553 and 11972175) are gratefully acknowledged. The authors are grateful for the helpful discussions with X.I.A. Yang, C.-X. Xu, W.-X. Huang, G. Yin and C.-Y. Wang, as well as M. Lee, R. Moser, S. Hoyas, J. Jiménez and C. Meneveau for making the channel DNS data publicly available. And R.H. would also like to acknowledge the inspiring communications with W. J. Baars.

## REFERENCES

- ABE, H., KAWAMURA, H. & CHOI, H. 2004 Very large-scale structures and their effects on the wall shear-stress fluctuations in a turbulent channel flow up to  $Re_\tau = 640$ . *J. Fluids Eng.* **126** (5), 835–843.
- ADRIAN, R. J. 2007 Hairpin vortex organization in wall turbulence. *Phys. Fluids* **19** (4), 041301.
- ADRIAN, R. J., MEINHART, C. D. & TOMKINS, C. D. 2000 Vortex organization in the outer region of the turbulent boundary layer. *J. Fluid Mech.* **422**, 1–54.
- AFZAL, N. & YAJNIK, K. 1973 Analysis of turbulent pipe and channel flows at moderately large Reynolds number. *J. Fluid Mech.* **61** (1), 23–31.
- AGOSTINI, L. & LESCHZINER, M. A. 2014 On the influence of outer large-scale structures on near-wall turbulence in channel flow. *Phys. Fluids* **26** (7), 075107.
- AGOSTINI, L. & LESCHZINER, M. A. 2016 Predicting the response of small-scale near-wall turbulence to large-scale outer motions. *Phys. Fluids* **28** (1), 015107.
- AGOSTINI, L., LESCHZINER, M. A. & GAITONDE, D. 2016 Skewness-induced asymmetric modulation of small-scale turbulence by large-scale structures. *Phys. Fluids* **28** (1), 015110.
- ANTONIA, R. A. & KIM, J. 1994 Low-Reynolds-number effects on near-wall turbulence. *J. Fluid Mech.* **276**, 61–80.
- ANTONIA, R. A., TEITEL, M., KIM, J. & BROWNE, L. W. B. 1992 Low-Reynolds-number effects in a fully developed turbulent channel flow. *J. Fluid Mech.* **236**, 579–605.
- BAARS, W. J., HUTCHINS, N. & MARUSIC, I. 2016 Spectral stochastic estimation of high-Reynolds-number wall-bounded turbulence for a refined inner-outer interaction model. *Phys. Rev. Fluids* **1** (5), 054406.
- BAARS, W. J. & MARUSIC, I. 2020a Data-driven decomposition of the streamwise turbulence kinetic energy in boundary layers. Part 1: Energy spectra. *J. Fluid Mech.* **882**, A25.
- BAARS, W. J. & MARUSIC, I. 2020b Data-driven decomposition of the streamwise turbulence

- kinetic energy in boundary layers. Part 2: Integrated energy and  $A_1$ . *J. Fluid Mech.* **882**, A26.
- BAARS, W. J., TALLURU, K. M., HUTCHINS, N. & MARUSIC, I. 2015 Wavelet analysis of wall turbulence to study large-scale modulation of small scales. *Exp. Fluids* **56** (10), 188.
- BALAKUMAR, B. J. & ADRIAN, R. J. 2007 Large- and very-large-scale motions in channel and boundary-layer flows. *Phil. Trans. R. Soc. A* **365** (1852), 665–681.
- BERNARDINI, M., PIROZZOLI, S. & ORLANDI, P. 2014 Velocity statistics in turbulent channel flow up to  $Re_\tau = 4000$ . *J. Fluid Mech.* **742**, 171–191.
- BRANDT, L. 2014 The lift-up effect: the linear mechanism behind transition and turbulence in shear flows. *Eur. J. Mech. B-Fluid* **47**, 80–96.
- BROWN, G. L. & THOMAS, A. S. W. 1977 Large structure in a turbulent boundary layer. *Phys. Fluids* **20** (10), S243–S252.
- BUTLER, K. M. & FARRELL, B. F. 1993 Optimal perturbations and streak spacing in wall-bounded turbulent shear flow. *Phys. Fluids A* **5** (3), 774–777.
- CARNEY, S. P., ENGQUIST, B. & MOSER, R. D. 2019 Near wall patch representation of wall bounded turbulence. *arXiv preprint arXiv:1910.06957*.
- CHEN, X., HUSSAIN, F. & SHE, Z.-S. 2018 Quantifying wall turbulence via a symmetry approach. Part 2. Reynolds stresses. *J. Fluid Mech.* **850**, 401–438.
- CHEN, X., HUSSAIN, F. & SHE, Z.-S. 2019 Non-universal scaling transition of momentum cascade in wall turbulence. *J. Fluid Mech.* **871**, R2.
- CHENG, C., LI, W., LOZANO-DURÁN, A. & LIU, H. 2019 Identity of attached eddies in turbulent channel flows with bidimensional empirical mode decomposition. *J. Fluid Mech.* **870**, 1037–1071.
- CHING, C. Y., DJENIDI, L. & ANTONIA, R. A. 1995 Low-Reynolds-number effects in a turbulent boundary layer. *Exp. Fluids* **19**, 61–68.
- DE GRAAFF, DAVID B. & EATON, JOHN K. 2000 Reynolds-number scaling of the flat-plate turbulent boundary layer. *J. Fluid Mech.* **422**, 319–346.
- DEL ÁLAMO, J. C. & JIMÉNEZ, J. 2003 Spectra of the very large anisotropic scales in turbulent channels. *Phys. Fluids* **15** (6), L41.
- DEL ÁLAMO, J. C., JIMÉNEZ, J., ZANDONADE, P. & MOSER, R. 2004 Scaling of the energy spectra of turbulent channels. *J. Fluid Mech.* **500**, 135.
- DEL ÁLAMO, J. C., JIMÉNEZ, J., ZANDONADE, P. & MOSER, R. D. 2006 Self-similar vortex clusters in the turbulent logarithmic region. *J. Fluid Mech.* **561**, 329–358.
- DENNIS, D. J. C. & NICKELS, T. B. 2011 Experimental measurement of large-scale three-dimensional structures in a turbulent boundary layer. Part 1. Vortex packets. *J. Fluid Mech.* **673**, 180–217.
- DUAN, Y., ZHANG, P., ZHONG, Q., ZHU, D. & LI, D. 2020 Characteristics of wall-attached motions in open channel flows. *Phys. Fluids* **32** (5), 055110.
- EITEL-AMOR, G., ÖRLÜ, R., SCHLATTER, P. & FLORES, O. 2015 Hairpin vortices in turbulent boundary layers. *Phys. Fluids* **27** (2), 025108.
- ELLINGSEN, T. & PALM, E. 1975 Stability of linear flow. *Phys. Fluids* **18** (4), 487–488.
- ERM, L. & JOUBERT, P. N. 1991 Low-Reynolds-number turbulent boundary layers. *J. Fluid Mech.* **230**, 1–44.
- FERNHOLZ, H. & FINLEY, J. 1996 The incompressible zero-pressure-gradient turbulent boundary layer: an assessment of the data. *Prog. Aerospa. Sci.* **32** (4), 245–311.
- FRISCH, U. 1995 *Turbulence: the legacy of A. N. Kolmogorov*. Cambridge university press.
- GAO, Q., ORTIZ-DUENAS, C. & LONGMIRE, E. K. 2011 Analysis of vortex populations in turbulent wall-bounded flows. *J. Fluid Mech.* **678**, 87–123.
- GRAHAM, J., KANOV, K., YANG, X. I. A., LEE, M., MALAYA, N., LALESCU, C. C., BURNS, R., EYINK, G., SZALAY, A., MOSER, R. D. & MENEVEAU, C. 2016 A web services accessible database of turbulent channel flow and its use for testing a new integral wall model for LES. *J. Turbul.* **17** (2), 181–215.
- GUALA, M., HOMMEMA, S. E. & ADRIAN, R. J. 2006 Large-scale and very-large-scale motions in turbulent pipe flow. *J. Fluid Mech.* **554**, 521–542.
- GAD-EL HAK, M. & BANDYOPADHYAY, P. R. 1994 Reynolds number effects in wall-bounded turbulent flows. *Appl. Mech. Rev.* **47**, 307–365.

- HAMILTON, J. M., KIM, J. & WALEFFE, F. 1995 Regeneration mechanisms of near-wall turbulence structures. *J. Fluid Mech.* **287**, 317–348.
- HEAD, M. R. & BANDYOPADHYAY, P. 1981 New aspects of turbulent boundary-layer structure. *J. Fluid Mech.* **107**, 297–338.
- HEARST, R. J., DOGAN, E. & GANAPATHISUBRAMANI, B. 2018 Robust features of a turbulent boundary layer subjected to high-intensity free-stream turbulence. *J. Fluid Mech.* **851**, 416–435.
- HOYAS, S. & JIMÉNEZ, J. 2006 Scaling of the velocity fluctuations in turbulent channels up to  $Re_\tau = 2003$ . *Phys. Fluids* **18** (1), 011702.
- HU, R., WANG, L., WANG, P., WANG, Y. & ZHENG, X. 2018 Application of high-order compact difference scheme in the computation of incompressible wall-bounded turbulent flows. *Computation* **6** (2), 31.
- HU, R., YANG, X. I. A. & ZHENG, X. 2020 Wall-attached and wall-detached eddies in wall-bounded turbulent flows. *J. Fluid Mech.* **885**, A30.
- HU, R. & ZHENG, X. 2018 Energy contributions by inner and outer motions in turbulent channel flows. *Phys. Rev. Fluids* **3** (8), 084607.
- HULTMARK, M., BAILEY, S. C. C. & SMITS, A. J. 2010 Scaling of near-wall turbulence in pipe flow. *J. Fluid Mech.* **649**, 103–113.
- HULTMARK, M., VALLIKIVI, M., BAILEY, S. C. C. & SMITS, A. J. 2012 Turbulent pipe flow at extreme Reynolds numbers. *Phys. Rev. Lett.* **108** (9), 094501.
- HUTCHINS, N. & MARUSIC, I. 2007a Evidence of very long meandering features in the logarithmic region of turbulent boundary layers. *J. Fluid Mech.* **579**, 1–28.
- HUTCHINS, N. & MARUSIC, I. 2007b Large-scale influences in near-wall turbulence. *Phil. Trans. R. Soc. A* **365** (1852), 647–664.
- HWANG, J., LEE, J., SUNG, H. J. & ZAKI, T. A. 2016 Inner–outer interactions of large-scale structures in turbulent channel flow. *J. Fluid Mech.* **790**, 128–157.
- HWANG, J. & SUNG, H. J. 2018 Wall-attached structures of velocity fluctuations in a turbulent boundary layer. *J. Fluid Mech.* **856**, 958–983.
- HWANG, Y. 2013 Near-wall turbulent fluctuations in the absence of wide outer motions. *J. Fluid Mech.* **723**, 264–288.
- HWANG, Y. 2015 Statistical structure of self-sustaining attached eddies in turbulent channel flow. *J. Fluid Mech.* **767**, 254–289.
- HWANG, Y. 2016 Mesolayer of attached eddies in turbulent channel flow. *Phys. Rev. Fluids* **1**, 064401.
- INOUE, M., MATHIS, R., MARUSIC, I. & PULLIN, D. I. 2012 Inner-layer intensities for the flat-plate turbulent boundary layer combining a predictive wall-model with large-eddy simulations. *Phys. Fluids* **24** (7), 075102.
- JEONG, J., HUSSAIN, F., SCHOPPA, W. & KIM, J. 1997 Coherent structures near the wall in a turbulent channel flow. *J. Fluid Mech.* **332**, 185–214.
- JIMÉNEZ, J. 2018 Coherent structures in wall-bounded turbulence. *J. Fluid Mech.* **842**, P1.
- JIMÉNEZ, J. & HOYAS, S. 2008 Turbulent fluctuations above the buffer layer of wall-bounded flows. *J. Fluid Mech.* **611**, 215–236.
- JIMÉNEZ, J. & MOIN, P. 1991 The minimal flow unit in near-wall turbulence. *J. Fluid Mech.* **225**, 213–240.
- JIMÉNEZ, J. & MOSER, R. D. 2007 What are we learning from simulating wall turbulence? *Phil. Trans. R. Soc. A* **365** (1852), 715–732.
- JIMÉNEZ, J. & PINELLI, A. 1999 The autonomous cycle of near-wall turbulence. *J. Fluid Mech.* **389**, 335–359.
- JODAI, Y. & ELSINGA, G. E. 2016 Experimental observation of hairpin auto-generation events in a turbulent boundary layer. *J. Fluid Mech.* **795**, 611–633.
- KAWAHARA, G. & KIDA, S. 2001 Periodic motion embedded in plane Couette turbulence: regeneration cycle and burst. *J. Fluid Mech.* **449**, 291–300.
- KIM, J. & MOIN, P. 1986 The structure of the vorticity field in turbulent channel flow. Part 2. Study of ensemble-averaged fields. *J. Fluid Mech.* **162**, 339–363.
- KIM, J., MOIN, P. & MOSER, R. 1987 Turbulence statistics in fully developed channel flow at low Reynolds number. *J. Fluid Mech.* **177**, 133–166.

- KIM, K. C. & ADRIAN, R. J. 1999 Very large-scale motion in the outer layer. *Phys. Fluids* **11** (2), 417–422.
- KLEWICKI, J. C. 2010 Reynolds number dependence, scaling, and dynamics of turbulent boundary layers. *J. Fluids Eng.* **132** (9).
- KLINE, S. J., REYNOLDS, W. C., SCHRAUB, F. A. & RUNSTADLER, P. W. 1967 The structure of turbulent boundary layers. *J. Fluid Mech.* **30** (4), 741–773.
- KOLMOGOROV, A. N. 1941 The local structure of turbulence in incompressible viscous fluid for very large Reynolds numbers. *C.R. Acad. Sci. U.R.S.S.* **30**, 301–305.
- KOVASZNAY, L. S. G., KIBENS, V. & BLACKWELDER, R. F. 1970 Large-scale motion in the intermittent region of a turbulent boundary layer. *J. Fluid Mech.* **41** (2), 283–325.
- LANDAHL, M. T. 1990 On sublayer streaks. *J. Fluid Mech.* **212**, 593–614.
- LEE, C. & JIANG, X. 2019 Flow structures in transitional and turbulent boundary layers. *Phys. Fluids* **31** (11), 111301.
- LEE, J. H. & SUNG, H. J. 2011 Very-large-scale motions in a turbulent boundary layer. *J. Fluid Mech.* **673**, 80–120.
- LEE, M. K. & MOSER, R. D. 2015 Direct numerical simulation of turbulent channel flow up to  $Re_\tau \approx 5200$ . *J. Fluid Mech.* **774**, 395–415.
- LEE, M. K. & MOSER, R. D. 2019 Spectral analysis of the budget equation in turbulent channel flows at high Reynolds number. *J. Fluid Mech.* **860**, 886–938.
- LOZANO-DURÁN, A., FLORES, O. & JIMÉNEZ, J. 2012 The three-dimensional structure of momentum transfer in turbulent channels. *J. Fluid Mech.* **694**, 100–130.
- LU, S. S. & WILLMARTH, W. W. 1973 Measurements of the structure of the Reynolds stress in a turbulent boundary layer. *J. Fluid Mech.* **60** (3), 481–511.
- MARUSIC, I., BAARS, W. J. & HUTCHINS, N. 2017 Scaling of the streamwise turbulence intensity in the context of inner-outer interactions in wall turbulence. *Phys. Rev. Fluids* **2** (10), 100502.
- MARUSIC, I., CHAUHAN, K. A., KULANDAIVELU, V. & HUTCHINS, N. 2015 Evolution of zero-pressure-gradient boundary layers from different tripping conditions. *J. Fluid Mech.* **783**, 379–411.
- MARUSIC, I., MATHIS, R. & HUTCHINS, N. 2010a Predictive model for wall-bounded turbulent flow. *Science* **329** (5988), 193–196.
- MARUSIC, I., MCKEON, B. J., MONKEWITZ, P. A., NAGIB, H. M., SMITS, A. J. & SREENIVASAN, K. R. 2010b Wall-bounded turbulent flows at high Reynolds numbers: Recent advances and key issues. *Phys. Fluids* **22** (6), 065103.
- MARUSIC, I. & MONTY, J. P. 2019 Attached eddy model of wall turbulence. *Annu. Rev. Fluid Mech.* **51**, 49–74.
- MARUSIC, I., MONTY, J. P., HULTMARK, M. & SMITS, A. J. 2013 On the logarithmic region in wall turbulence. *J. Fluid Mech.* **716**, R3.
- MATHIS, R., HUTCHINS, N. & MARUSIC, I. 2009 Large-scale amplitude modulation of the small-scale structures in turbulent boundary layers. *J. Fluid Mech.* **628**, 311–337.
- MATHIS, R., HUTCHINS, N. & MARUSIC, I. 2011 A predictive inner-outer model for streamwise turbulence statistics in wall-bounded flows. *J. Fluid Mech.* **681**, 537–566.
- MEHREZ, A., PHILIP, J., YAMAMOTO, Y. & TSUJI, Y. 2019 Pressure and spanwise velocity fluctuations in turbulent channel flows: Logarithmic behavior of moments and coherent structures. *Phys. Rev. Fluids* **4**, 044601.
- METZGER, M. M. & KLEWICKI, J. C. 2001 A comparative study of near-wall turbulence in high and low Reynolds number boundary layers. *Phys. Fluids* **13** (3), 692.
- MILLIKAN, C. B. 1939 A critical discussion of turbulent flow in channels and circular tubes. In *Proceedings of the 5th International Congress on Applied Mechanics*, pp. 386–392. Wiley.
- MIZUNO, Y. & JIMÉNEZ, J. 2011 Mean velocity and length-scales in the overlap region of wall-bounded turbulent flows. *Phys. Fluids* **23** (8), 085112.
- MOCHIZUKI, S. & NIEUWSTADT, F. T. M. 1996 Reynolds-number-dependence of the maximum in the streamwise velocity fluctuations in wall turbulence. *Exp. Fluids* **21** (3), 218–226.
- MONKEWITZ, P. A. & NAGIB, H. M. 2015 Large-Reynolds-number asymptotics of the streamwise normal stress in zero-pressure-gradient turbulent boundary layers. *J. Fluid Mech.* **783**, 474–503.

- MORRISON, J. F. 2007 The interaction between inner and outer regions of turbulent wall-bounded flow. *Phil. Trans. R. Soc. A* **365** (1852), 683–698.
- MORRISON, J. F., MCKEON, B. J., JIANG, W. & SMITS, A. J. 2004 Scaling of the streamwise velocity component in turbulent pipe flow. *J. Fluid Mech.* **508**, 99.
- PAN, C. & KWON, Y. 2018 Extremely high wall-shear stress events in a turbulent boundary layer. *J. Phys.: Conf. Ser.* **1001**, 012004.
- PERRY, A. E. & ABELL, C. J. 1975 Scaling laws for pipe-flow turbulence. *J. Fluid Mech.* **67**, 257–271.
- PERRY, A. E. & CHONG, M. S. 1982 On the mechanism of wall turbulence. *J. Fluid Mech.* **119**, 173–217.
- PERRY, A. E. & MARUSIC, I. 1995 A wall-wake model for the turbulence structure of boundary layers. part 1. extension of the attached eddy hypothesis. *J. Fluid Mech.* **298**, 361–388.
- PURTELL, L. P., KLEBANOFF, P. S. & BUCKLEY, F. T. 1981 Turbulent boundary layer at low Reynolds number. *Phys. Fluids A* **24**, 802–811.
- ROBINSON, S. K. 1991 Coherent motions in the turbulent boundary layer. *Annu. Rev. Fluid Mech.* **23**, 601–639.
- SAMIE, M., MARUSIC, I., HUTCHINS, N., FU, M. K., FAN, Y., HULTMARK, M. & SMITS, A. J. 2018 Fully resolved measurements of turbulent boundary layer flows up to  $Re_\tau = 20\,000$ . *J. Fluid Mech.* **851**, 391–415.
- SCHLATTER, P., LI, Q., ÖRLÜ, R., HUSSAIN, F. & HENNINGSON, D. S. 2014 On the near-wall vortical structures at moderate Reynolds numbers. *Eur. J. Mech. B-Fluid* **48**, 75–93.
- SCHOPPA, W. & HUSSAIN, F. 2002 Coherent structure generation in near-wall turbulence. *J. Fluid Mech.* **453**, 57–108.
- SCHULTZ, M. P. & FLACK, K. A. 2013 Reynolds-number scaling of turbulent channel flow. *Phys. Fluids* **25** (2), 025104.
- SHEKAR, A. & GRAHAM, M. D. 2018 Exact coherent states with hairpin-like vortex structure in channel flow. *J. Fluid Mech.* **849**, 76–89.
- SHENG, J., MALKIEL, E. & KATZ, J. 2009 Buffer layer structures associated with extreme wall stress events in a smooth wall turbulent boundary layer. *J. Fluid Mech.* **633**, 17–60.
- SILLERO, J. A., JIMÉNEZ, J. & MOSER, R. D. 2013 One-point statistics for turbulent wall-bounded flows at Reynolds numbers up to  $\delta^+ \approx 2000$ . *Phys. Fluids* **25** (10), 105102.
- SMITH, C. R. & METZLER, S. P. 1983 The characteristics of low-speed streaks in the near-wall region of a turbulent boundary layer. *J. Fluid Mech.* **129**, 27–54.
- SMITS, A. J., MCKEON, B. J. & MARUSIC, I. 2011 High-Reynolds number wall turbulence. *Annu. Rev. Fluid Mech.* **43**, 353–375.
- SPALART, P. R. 1988 Direct simulation of a turbulent boundary layer up to  $R_\theta = 1410$ . *J. Fluid Mech.* **187**, 61–98.
- STANISLAS, M. 2017 Near wall turbulence: An experimental view. *Phys. Rev. Fluids* **2** (10), 100506.
- TACHIE, M. F., BALACHANDAR, R. & BERGSTROM, D. J. 2003 Low Reynolds number effects in open-channel turbulent boundary layers. *Exp. Fluids* **34**, 616–624.
- TALLURU, K. M., BAIDYA, R., HUTCHINS, N. & MARUSIC, I. 2014 Amplitude modulation of all three velocity components in turbulent boundary layers. *J. Fluid Mech.* **746**, R1.
- TENNEKES, H. & LUMLEY, J. L. 1972 *A first course in turbulence*. MIT Press.
- TOWNSEND, A. 1976 *The structure of turbulent shear flow*. Cambridge University Press.
- VALLIKIVI, M., GANAPATHISUBRAMANI, B. & SMITS, A. J. 2015a Spectral scaling in boundary layers and pipes at very high Reynolds numbers. *J. Fluid Mech.* **771**, 303–326.
- VALLIKIVI, M., HULTMARK, M. & SMITS, A. J. 2015b Turbulent boundary layer statistics at very high Reynolds number. *J. Fluid Mech.* **779**, 371–389.
- VINCENTI, P., KLEWICKI, J., MORRILL-WINTER, C., WHITE, C. M. & WOSNIK, M. 2013 Streamwise velocity statistics in turbulent boundary layers that spatially develop to high Reynolds number. *Exp. Fluids* **54** (12), 1629.
- WALEFFE, F. 1997 On a self-sustaining process in shear flows. *Phys. Fluids* **9** (4), 883–900.
- WALEFFE, F. 2001 Exact coherent structures in channel flow. *J. Fluid Mech.* **435**, 93.
- WALLACE, J. M. 2016 Quadrant analysis in turbulence research: history and evolution. *Annu. Rev. Fluid Mech.* **48**, 131–158.

- WALLACE, J. M., ECKELMANN, H. & BRODKEY, R. S. 1972 The wall region in turbulent shear flow. *J. Fluid Mech.* **54** (1), 39–48.
- WANG, C., GAO, Q., WANG, J., WANG, B. & PAN, C. 2019a Experimental study on dominant vortex structures in near-wall region of turbulent boundary layer based on tomographic particle image velocimetry. *J. Fluid Mech.* **874**, 426–454.
- WANG, G. & ZHENG, X. 2016 Very large scale motions in the atmospheric surface layer: a field investigation. *J. Fluid Mech.* **802**, 464–489.
- WANG, H.-P., WANG, S.-Z. & HE, G.-W. 2018 The spanwise spectra in wall-bounded turbulence. *Act. Mech. Sin.* **34** (3), 452–461.
- WANG, W., PAN, C. & WANG, J. 2019b Wall-normal variation of spanwise streak spacing in turbulent boundary layer with low-to-moderate Reynolds number. *Entropy* **21** (1), 24.
- WANG, Y., HUANG, W. & XU, C. 2015 On hairpin vortex generation from near-wall streamwise vortices. *Act. Mech. Sin.* **31** (2), 139–152.
- WEI, T. & WILLMARTH, W. W. 1989 Reynolds-number effects on the structure of a turbulent channel flow. *J. Fluid Mech.* **204**, 57–95.
- WILLERT, C. E., SORIA, J., STANISLAS, M., KLINNER, J., AMILI, O., EISFELDER, M., CUVIER, C., BELLANI, G., FIORINI, T. & TALAMELLI, A. 2017 Near-wall statistics of a turbulent pipe flow at shear Reynolds numbers up to 40,000. *J. Fluid Mech.* **826**.
- WILLMARTH, W. W. & LU, S. S. 1972 Structure of the Reynolds stress near the wall. *J. Fluid Mech.* **55** (1), 65–92.
- WU, X. & MOIN, P. 2009 Direct numerical simulation of turbulence in a nominally zero-pressure-gradient flat-plate boundary layer. *J. Fluid Mech.* **630**, 5–41.
- YAMAMOTO, Y. & TSUJI, Y. 2018 Numerical evidence of logarithmic regions in channel flow at  $Re_\tau = 8000$ . *Phys. Rev. Fluids* **3** (1), 012602.
- YANG, X. I. A., BAIDYA, R., LV, Y. & MARUSIC, I. 2018 Hierarchical random additive model for the spanwise and wall-normal velocities in wall-bounded flows at high Reynolds numbers. *Phys. Rev. Fluids* **3** (12), 124606.
- YANG, Y. & PULLIN, D. I. 2011 Geometric study of Lagrangian and Eulerian structures in turbulent channel flow. *J. Fluid Mech.* **674**, 67–92.
- YIN, G., HUANG, W.-X. & XU, C.-X. 2017 On near-wall turbulence in minimal flow units. *Int. J. Heat Fluid Flow* **65**, 192–199.
- YIN, G., HUANG, W.-X. & XU, C.-X. 2018 Prediction of near-wall turbulence using minimal flow unit. *J. Fluid Mech.* **841**, 654–673.
- ZHOU, J., ADRIAN, R. J., BALACHANDAR, S. & KENDALL, T. M. 1999 Mechanisms for generating coherent packets of hairpin vortices in channel flow. *J. Fluid Mech.* **387**, 353–396.